



Cross-shore Deformation of a Surfzone Released Dye Plume by an Internal Tide on the Inner-shelf.

DEREK J. GRIMES¹, FALK FEDDERSEN¹, SARAH N. GIDDINGS¹, AND GENO
PAWLAK²

¹*Scripps Institution of Oceanography, La Jolla, California, USA*

²*University of California San Diego, La Jolla, California, USA*

Journal of Physical Oceanography, submitted

October 11, 2019

Corresponding author address:

Derek J. Grimes, Scripps Institution of Oceanography, UCSD, 9500 Gilman Dr., La Jolla, CA
92093-0209, dgrimes@ucsd.edu

Early Online Release: This preliminary version has been accepted for publication in *Journal of the Physical Oceanography*, may be fully cited, and has been assigned DOI 10.1175/JPO-D-19-0046.1. The final typeset copyedited article will replace the EOR at the above DOI when it is published.

ABSTRACT

An inner-shelf (IS) dye plume that formed following a 3.84 h early morning surfzone (SZ) dye release off of Imperial Beach, CA is analyzed with in situ and aerial remotely-sensed observations. Mid morning, 5 h after release start, the IS-plume extended 800 m offshore (or $\approx 8L_{SZ}$, where L_{SZ} is the surfzone width) and was surface intensified. Over the next ≈ 2 h, the IS-plume deformed (narrowed) cross-shore with the offshore front progressing onshore at $\approx 5 \text{ cm s}^{-1}$, deepened by up to 3 m, and elongated along-shore at $\approx 4.5 \text{ cm s}^{-1} \text{ km}^{-1}$ (at $\approx 2.5L_{SZ}$). Coincident with IS-plume deformation and deepening, IS isotherms also deepened, with relatively stable IS-plume joint dye and temperature statistics. Offshore tracer transport and subsequent IS-plume deformation and deepening likely resulted from two phases of the diurnal internal tide (DIT). During and after deformation, the IS-plume did not re-enter the warm surfzone, which potentially acted as a thermal barrier. High-frequency internal waves (HF IW) propagated through the IS-plume at $\approx 9 \text{ cm s}^{-1}$ and dissipated onshore of $4L_{SZ}$. Surface HF IW signal was elevated in the plume elongation region, suggesting a linkage between plume elongation and either the DIT or HF IW. This IS-plume evolution differs from previous SZ tracer releases, highlighting the effects of release timing relative to the solar cycle or the internal tide.

1. Introduction

1 The cross-shore exchange of tracers across the surfzone (SZ, region of depth limited surface
2 gravity wave breaking) and the inner-shelf (IS, region offshore of surfzone to ≈ 15 m water depth)
3 is integral to coastal human and ecosystem health (*e.g.*, Barbier et al. 2011). For example, the
4 transfer of human pathogens across the SZ onto the IS dilutes SZ concentrations and improves
5 degraded coastal water quality (*e.g.*, Grant et al. 2005). Shoreward larval transport from the shelf
6 to inner-SZ intertidal recruitment sites is critical to coastal ecosystems (*e.g.*, Pineda et al. 2007).
7 Broadly, many different mechanisms are known to contribute to cross-shore exchange of tracers,
8 *i.e.*, across either SZ, IS, or both (*e.g.*, Morgan et al. 2018; Washburn and McPhee-Shaw 2013;
9 Lentz and Fewings 2012). However, the interaction and combination of both SZ and IS processes
10 across a range of timescales (such as, rip-currents and internal waves and tides) and their effect on
11 cross-shore tracer exchange is poorly understood.

12 SZ tracer dispersion is predominantly driven by breaking surface gravity waves. Dissipation
13 of surface gravity waves supplies turbulence (*e.g.*, Feddersen 2012), vertically mixing both tem-
14 perature and tracers (*e.g.*, Hally-Rosendahl et al. 2014). Breaking waves also drive SZ alongshore
15 currents (*e.g.*, Longuet-Higgins 1970a,b) and vertical vorticity (Clark et al. 2012). For alongshore
16 uniform nearshore morphologies (Feddersen and Guza 2003), tracer exchange does not gener-
17 ally depend on the alongshore location of tracer release, but may be sensitive to the release time.
18 Alongshore uniform cross-SZ tracer dispersion is attributed to SZ vertical eddy vorticity (Clark
19 et al. 2010). In contrast, for alongshore variable rip-channeled SZs, short timescale (< 90 s) drifter
20 dispersion is attributed to the strong shear in bathymetrically controlled rip currents (Brown et al.
21 2009).

22 SZ processes also drive exchange with and across the IS. For example, SZ eddies coalesce
23 to form transient rip-currents (TRC), ephemeral offshore directed flows that eject SZ water onto
24 the IS (*e.g.*, Johnson and Pattiaratchi 2004), and have been identified as irregular-alongshore dye
25 patches on the IS following a late-morning SZ dye release (Hally-Rosendahl et al. 2014). TRCs
26 brought SZ released dye out to $2L_{sz}$ - $3L_{sz}$ (where L_{sz} is the width of the SZ) offshore in about 5 h
27 (Hally-Rosendahl et al. 2015). In barotropic models, TRC driven exchange can be significantly
28 larger than Stokes drift exchange up to several SZ widths from shore, and depends critically on
29 incident wave directional spread (Suanda and Feddersen 2015). On the stratified IS, TRCs can
30 enhance vertical mixing, generating a baroclinic cross-shore circulation (Kumar and Feddersen
31 2017a) that induces a subsurface cross-shore tracer exchange pathway out to $6L_{sz}$ - $8L_{sz}$ over 12 h
32 (Kumar and Feddersen 2017b). On rip-channeled beaches, bathymetrically controlled rip currents
33 can circulate water between the SZ and IS, in some cases with little net cross-shore exchange due
34 to recirculation (*e.g.*, Brown et al. 2015).

35 In addition to SZ generated TRCs, other processes—spanning a large range of time and space
36 scales—contribute to cross-shore exchange on an alongshore uniform IS (*e.g.*, Lentz and Few-
37 ings 2012). On relatively long subtidal (> 33 h) timescales, alongshore upwelling (downwelling)
38 winds can drive cross-shelf circulation on the mid to outer shelf (*e.g.*, Smith 1981). On the shal-
39 low IS, cross-shore circulation is weaker and may shut down under unstratified conditions, poten-
40 tially blocking IS tracer exchange (Lentz 2001; Austin and Lentz 2002). Cross-shore winds also
41 contribute to cross-shelf circulation with response dependent on initial vertical and cross-shore
42 stratification (Horwitz and Lentz 2014).

43 On the mid-shelf, semi-diurnal and diurnal tidal-band internal waves have been inferred to
44 induce cross-shelf nutrient fluxes (Lucas et al. 2011). On the shallow IS, internal waves can drive

45 considerable temperature fluctuations, even at $h = 5$ m depth (Winant 1974), and induce exchange
46 (Pineda 1999). Near-bed cold bores with timescales 1-4 h have been observed to propagate upslope
47 from 8 m to 2 m depth (outer SZ limit) in a manner consistent with an upslope gravity current
48 (Sinnott et al. 2018). High-frequency internal waves (HF IW, periods ≤ 1 h) in the form of solitary-
49 like waves are often associated with these bores (*e.g.*, Walter et al. 2012; Klymak and Moum 2003).
50 Instability of large amplitude internal tides (IT) can generate smaller scale (and higher-frequency)
51 IWs (*e.g.*, Holloway et al. 1999) that can contribute to cross-shelf mass flux (*e.g.*, Lamb 1997;
52 Shroyer et al. 2010; Zhang et al. 2015). Thus, internal waves at tidal and HF timescales may
53 contribute to exchange across the IS and potentially even across the SZ.

54 Cross-shore buoyancy gradients can also influence IS exchange. For instance, nearshore di-
55 urnal heating and cooling drives exchange (*e.g.*, Monismith et al. 1990; Farrow and Patterson
56 1993), with potential to flush the SZ-IS region in roughly a day (Molina et al. 2014). Vertical
57 shear in alongshore flows can also result in Coriolis-driven cross-shore exchange (Ulloa et al.
58 2018). Alternatively, a strong SZ/IS temperature difference (*e.g.*, mid-day warmer SZ and colder
59 IS, Hally-Rosendahl et al. 2014) may prevent IW propagation into very shallow water (*i.e.*, < 4 m
60 depth, *e.g.*, Omand et al. 2011).

61 Several previous SZ dye releases observed cross-shore tracer dispersal onto the IS to $2L_{sz}$ - $3L_{sz}$
62 over 2-5 h (*e.g.*, Grant et al. 2005; Hally-Rosendahl et al. 2014, 2015). However, the mechanism
63 for exchanging tracer farther offshore is not clear and likely involves IS processes across a range of
64 spatiotemporal scales (*e.g.*, HF IW and IT, and diurnal thermal exchange). Furthermore, because
65 these previous SZ dye releases were all mid- to late-morning in either May or September in South-
66 ern California (with strong solar heating), the effect of release timing on the cross-shore exchange
67 is not clear. Previous IS tracer release experiments in $6 < h < 12$ m depth have focused on testing

68 relative dispersion scalings (*e.g.*, Stacey et al. 2000; Fong and Stacey 2003; Jones et al. 2008) and
69 underlying mechanisms, like shear-dispersion (*e.g.*, Sundermeyer and Ledwell 2001; Moniz et al.
70 2014).

71 Under realistic conditions, a combination of IS processes with a range of spatiotemporal scales
72 are likely to contribute to IS tracer exchange, which can make field observations difficult to con-
73 textualize. For example, large-scale stratification changes during tracer observations (*e.g.*, Fong
74 and Stacey 2003) can bias dispersion statistics. Even for nearly stationary conditions, the number
75 of independent realizations often is logistically limited, precluding statistical treatment. Addition-
76 ally, limited observations can make it difficult to attribute the observed tracer evolution to physical
77 processes (*e.g.*, Sundermeyer and Ledwell 2001). Observations of tracer evolution spanning the
78 range of scales (*e.g.*, TRCs to HF IW to IT) are necessary to understand how SZ released tracer is
79 exchanged across the IS.

80 As part of the Cross-Surfzone/Inner-shelf Dye Exchange (CSIDE) experiment (Imperial Beach,
81 California, Fig. 1a), the evolution of an early morning, SZ released tracer is observed on the IS over
82 ≈ 10 h and ≈ 10 km alongshore where tracer plume width varied from 500-800 m (or $5L_{sz}$ - $8L_{sz}$)
83 cross-shore. Dye, temperature, and current observations, as well as averaging methodologies are
84 described in Section 2. In Section 3, novel IS-plume observations from aerial remote and *in situ*
85 observations are presented. The effect of the internal tide, HF IW, and solar heating on the evolu-
86 tion of the IS tracer plume as well as the potential effect of shoreline tracer release timing relative
87 to internal tide phase and solar cycle are discussed in Section 4. The results are summarized in
88 Section 5.

2. Methods

89 The CSIDE study consisted of three dye tracer releases, conducted in the southern San Diego
90 Bight near the city of Imperial Beach (IB), California (Fig. 1) in fall of 2015. Herein we report on
91 IS observations spanning approximately 11.5 h following the start of the second release (R2) on 8
92 October 2015. The San Diego Bight region includes San Diego Bay and is bounded by the United
93 States/Mexico border and Tijuana River Estuary to the south, and Point Loma to the north and
94 west, and includes the cities of IB and Coronado. A broad shoal offshore of the estuary focuses
95 incoming swell (see the 6 and 12 m depth contour in Fig. 1a) resulting in locally complex wave
96 transformation patterns. Between IB and Coronado is a 9 km isthmus that includes Silver Strand
97 State Beach where the 6 and 12 meter depth contours are approximately parallel to shore. The
98 coastline curves more rapidly near Coronado before terminating at the N/S oriented San Diego
99 Bay Inlet. The local right-handed coordinate system originates at the location of the second re-
100 lease, R2 in Fig. 1a-b, with positive x increasing on-shore and oriented approximately true-east,
101 y oriented along-coast at the origin and toward north, and vertical coordinate z is up relative to
102 mean-sea-level. In addition, a local, shoreline referenced shore-normal coordinate is given by \tilde{x} ,
103 and \tilde{z} is used to denote vertical measurements relative to the tidally varying sea-surface η .

a. Moored and Fixed Instrumentation

104 Fixed instruments were deployed in the study region for approximately one month (15 Sept.–15
105 Oct. 2015) to provide regional scale physical oceanographic conditions (see Fig. 1a). Three moor-
106 ings provided water column temperature measurements. The southern-most mooring (Tr in Fig. 1)
107 was located approximately on the $h = 12$ m isobath and consisted of 6 Sea-Bird 56 thermistors

108 sampling at 0.5 Hz with vertical spacing $\Delta z = 1.5$ m beginning at $z = -2.6$ m below mean-
109 sea-level (MSL). A 1.2 MHz RD Instruments 4-beam acoustic Doppler current profiler (ADCP in
110 Fig. 1b) was deployed adjacent to mooring Tr ($\Delta x = 202$ m, $\Delta y = 195$ m) on roughly the 11 m
111 isobath. The ADCP sampled during daytime from 08:00-16:00 PDT with a sample rate of 1 Hz
112 and vertical resolution of 0.5 m. Farther north, two Wirewalker wave powered profilers (Rainville
113 and Pinkel 2001) outfitted with Sea-Bird-49 conductivity-temperature-depth (CTD) sensors and
114 Wetlab ECO-Triplet fluorometers (W1 & W2 in Fig. 1a) were deployed on the $h = 13$ & 14 m
115 bathymetry contour, respectively. These Wirewalkers sampled roughly the upper two-thirds of
116 the water column and under typical conditions repeat profiles took ≈ 90 s. Moorings W1 and
117 W2 were located about 1.4 km and 5.7 km from Tr, respectively with W1 and W2 separated by
118 4.3 km. Wave data was provided by Coastal Data Information Program (CDIP) IB West buoy
119 number 218 (CDIP in Fig. 1a). Wind speed and direction was provided by the Tijuana River Es-
120 tuary National Research Reserve meteorological station (denoted MET in Fig. 1a). Additional
121 instrumentation was deployed offshore and inside the Tijuana River Estuary that are not used in
122 this analysis.

b. Surfzone Dye Release

123 The R2 release period started at 05:18 PDT (hereafter time of day is presented as 0518 h, and
124 time since release start t_r is given in decimal hours) on 8 October 2015 and lasted approximately
125 3.84 h. A total of 113.6 L of 21.49% Rhodamine WT fluorescent dye solution was pumped via
126 a medical-grade peristaltic pump at a rate of ≈ 0.5 L min⁻¹ into the SZ at a fixed cross-shore
127 position where the depth varied from roughly 0.25 m to 0.75 m with the incoming tide over the

128 release duration. Dye release location temperature was measured with a Sea-Bird-56 thermistor at
129 1 Hz. The release was chosen to coincide with incident south swell (*i.e.*, driving SZ currents to
130 north) and the incoming phase of the surface tide (*i.e.*, during positive along-shore tidal velocity)
131 to maximize the potential for northward transport.

c. Mobile Instrumentation

132 Mobile observation began after the start of the dye release with SZ, *in situ* IS, and aerial remote-
133 sensed platforms (symbols and lines in Fig. 1b). SZ dye and temperature were measured at 1 Hz
134 for 48 h after release start with Wetlab ECO-Triplet fluorometer + temperature sensors mounted
135 to poles (S1-S3, Fig. 1b) and with co-located ECO-Triplet fluorometers + Sea-Bird-39 thermistors
136 mounted to anchored mobile carts (M1-M5, Fig. 1). These platforms were deployed mid-SZ. The
137 pole-mounted instruments were not moved once deployed, whereas the carts were moved cross-
138 shore with the tide to maintain roughly mid-SZ position.

139 *In situ* IS sampling consisted of vessel towed array (TA) and autonomous-underwater-vehicle
140 (AUV) transects (TA and AUV in Fig. 1b). The TA had 5 Wetlab ECO-Triplet fluorometer +
141 temperature sensors sampling at 1-6 m below the surface with a vertical spacing between 1-2 m.
142 The 2.5 km-long south-north TA transect (cyan and TA in Fig. 1b) was surveyed at approximately
143 0.6 m s^{-1} from 1107 h to 1210 h ($t_r = 5.80\text{-}6.85 \text{ h}$). The AUV was a REMUS-100 (Hydroid Inc.)
144 equipped with a Sea-Bird-49 CTD and Wetlabs ECO-Puck fluorometer. The AUV drove repeated
145 500-m long cross-shore and vertical transects (red line and AUV in Fig. 1b) between 0900-1200 h
146 ($t_r = 3.69\text{-}6.69 \text{ h}$). Two repeat cross-shore surveys, taking on average $\leq 20 \text{ min}$, were used
147 to generate (x, z) dye and temperature maps. A jet-ski sampled near-surface (20 cm) dye and

148 temperature in a mow-the-lawn pattern (not shown) that was used to calibrate aerial hyperspectral
149 measurements.

150 Aerial remote sensing with the Modular Aerial Sampling System (MASS, Melville et al. 2016)
151 was used to estimate georeferenced surface dye concentration and relative temperature. The dye
152 plume was imaged 53 times between 1020 – 1658 h ($t_r = 5.02\text{-}11.65$ h). Photo-mosaic relative
153 sea surface temperature was measured with an infrared camera (8.0-9.2 μm wavelength band).
154 Push-broom hyperspectral imagery spanning wavelengths of 400 – 990 nm in 126 bands was used
155 to estimate surface dye concentration. The raw hyperspectral data has a cross-track resolution of
156 roughly 1.25 m (depending on altitude) and was interpolated to a regular 2×2 m grid (likewise
157 for temperature). The hyperspectral imagery is converted to surface dye concentrations $D(x, y)$
158 (Fig. 2a), following Clark et al. (2014) by calibrating to coextensive *in situ* near-surface jet-ski dye
159 measurements (not shown). IS remote hyperspectral dye measurements are likely sensitive to dye
160 vertical structure, therefore this calibration ensures MASS dye estimates are representative of the
161 near-surface ($\tilde{z} \approx -20$ cm) dye concentration.

FIG. 4

d. Definition of Scales and Filtering

162 The dye and temperature fields varied over a broad range of horizontal length (meters to kilo-
163 meters) and time (minutes to days) scales, owing to the various processes across the SZ and IS.
164 The range of length scales is seen in the high spatial resolution aerial surface dye measurements
165 (*e.g.*, Fig. 2a). Similarly, moored temperature observations vary at a range of timescales, from
166 diurnal and semi-diurnal to periods of approximately 10 min. In the analyses of Section 3, dye
167 and temperature fields are decomposed into large- and small-scale fields, denoted by (\bar{D}, \bar{T}) and

168 (D', T') , respectively, using a spatial filter with cut-off of approximately 150 m, and results are
169 presented separately to highlight the dominant processes influencing the dye plume at each scale. FIG. 5

170 For a particular observation source, dye and temperature were filtered with the same method.
171 Aerial dye $D(x, y)$ and temperature $T(x, y)$ imagery were convolved with a two-dimensional
172 $150 \text{ m} \times 150 \text{ m}$ Hamming window. The AUV $D(x, z)$ & $T(x, z)$ transects were objectively mapped
173 using horizontal and vertical decorrelation scales of 150 m and 2 m, respectively. The TA $D(y, z)$
174 & $T(y, z)$ transect was smoothed via convolution with a Hamming window in the time-domain
175 equivalent to an average along-track length scale of approximately 150 m (*i.e.*, 4 min underway at
176 0.6 m s^{-1}). Mooring $T(t, z)$ and current meter cross-shore velocity $u(t, z)$ were convolved with a
177 30 min wide Hamming window. Results were not sensitive to the windowing function.

178 The linkage between the 150 m spatial scale filter cut-off and the 30 min time domain filter
179 cut-off is based on the shallow water and flat bottom, mode-1 linear internal wave (IW) dispersion
180 relationship,

$$\omega = k \frac{Nh}{\pi}, \quad (1)$$

181 where $N = (-g\rho_o^{-1}\partial\rho/\partial z)^{1/2}$ is the buoyancy frequency, h the local water depth, k is the local
182 wavenumber and ω the frequency of the IW. The vertical temperature time-series at Tr ($h = 12 \text{ m}$)
183 was used to compute $N(t, z)$, using a constant salinity of 33.4 PSU, resulting in the depth and
184 time (0800–1300 h) averaged $N = 2.3 \times 10^{-2} \text{ rad s}^{-1}$, or $2\pi/N = 4.5 \text{ min}$. Thus, an IW with a
185 wavelength of 150 m has a period of approximately 30 min. By applying a constant 150 m scale
186 spatial filter both HF IWs (periods 4.5–30 min) and TRCs were classified as small scale.

187 An example surface dye decomposition into large and small scales is shown in Fig. 2. The

188 large-scale (*i.e.*, > 150 m) dye field $\bar{D}(x, y)$ (Fig. 2b) captures the boundaries and the peak con-
189 centration of the plume. Small-scale (< 150 m) dye field $D'(x, y)$ (Fig. 2c) variations are roughly
190 ± 2 ppb, with signatures of wave breaking in the SZ, TRCs at the SZ/IS boundary, as well as HF
191 IW-like features on the IS.

3. Results

FIG. 6

a. Regional Observations and Dye Release Background Conditions

192 During the experiment, a diurnal sea-breeze was typical with onshore wind speeds of 5 m s^{-1} ,
193 peaking in the afternoon, along with a slight northerly mean of approximately 0.5 m s^{-1} (Fig. 3a).
194 On 4 & 5 October 2015 a storm interrupted this pattern with sustained 8 m s^{-1} southerly winds
195 (Fig. 3a) and 5 mm of precipitation (not shown). Atmospheric conditions returned to normal by
196 6 October. On 8 October (first day of R2), the CDIP buoy average significant wave height was
197 0.84 m (Fig. 3b), with peak period ≈ 14.3 s and peak direction ≈ 226 deg true (*i.e.*, from SW
198 and driving northward SZ currents). The maximum tidal range in the San Diego Bight is roughly
199 2 m. During R2, the tidal range was 1.4 m with a semi-diurnal inequality of approximately 20 cm
200 (Fig. 3c).

201 The mid-depth IS temperature variability had a prominent diurnal internal tidal (DIT) signature
202 (Fig. 3d) that was modulated sub-tidally. Over the 1 month, the diurnal mid-depth temperature
203 fluctuations (Fig. 3d) were coherent at a level of ≈ 0.8 between the three alongshore tempera-
204 ture moorings (*i.e.*, Tr, W1, and W2), with a north-to-south phase propagation of approximately
205 40 cm s^{-1} (see Fig. 3d). The IS stratification (not shown) was dominated by the vertical temper-

206 ature gradient, where the average temperature difference was 2.1 °C over a vertical distance of
207 7.5 m (not shown). During R2, the mid-depth temperature varied by 1.5 °C, and the dye release
208 (magenta, Fig. 3) occurred during the cooling phase of the DIT. Sub-inertial, diurnal internal waves
209 have previously been observed in the Southern California Bight region (*e.g.*, Nam and Send 2011;
210 Kumar et al. 2016). A diurnal sea-breeze can force diurnal band internal oscillations (*e.g.*, Walter
211 et al. 2017) that are potentially resonant if the effective inertial frequency is decreased due to shear
212 in sub-tidal alongshore currents (*e.g.*, Lerczak et al. 2001).

213 On the day of R2, the DIT both shoaled and relaxed isotherms at mooring Tr ($h = 12$ m,
214 Fig. 4a). Over the release period (magenta bar, top of Fig. 4a) the $T = 20.5$ °C isotherm shoaled
215 5.5 m over 3 h (dashed black line in Fig. 4a). Subsequently, the water column warmed, with the
216 $T = 20.5$ °C isotherm deepening about 0.6 m over 2 h (termed deformation period; gray bar, top
217 of Fig. 4a). The rapid cooling-then-warming at Tr was associated with a large-scale baroclinic
218 cross-shore velocity observed at ADCP that delivered cold water onshore at depth prior to and
219 during the release period and reversed during the deformation period (Fig. 4b). This large-scale
220 temperature fluctuation and velocity signature was observed at all three moorings (Tr, W1, W2).
221 Thermally driven exchange has diurnal temperature and cross-shore flow signals (Molina et al.
222 2014), however it does not set up an alongshore propagating wave motion (Fig. 3d) nor does it
223 have the observed mode-1 structure and phasing (Fig. 4b), thus is not a likely mechanism for the
224 observed diurnal signal.

225 The large-scale (> 30 min) and along-shore averaged SZ temperature, estimated from 9 ther-
226 mistors spanning 7 km alongshore (R2, S1-S3, and M1-M5 in Fig. 1), was dominated by the diurnal
227 heating/cooling cycle (Fig. 4c). The SZ root-mean-square (rms) deviations from the alongshore av-
228 erage (gray shading, Fig. 4c) were small (< 0.2 °C) prior to the deformation period. During the

229 first half of the release period, the R2 location temperature (T_{rel} , magenta in Fig. 4c) was on av-
230 erage ≈ 0.5 °C colder than the Tr mooring $z = -2.7$ m thermistor (blue, Fig. 4c). This is likely
231 a lower bound for the cross-shore temperature difference between the SZ and Tr, because for a
232 well-mixed SZ with an average depth of 1 m, a thermistor at this z -level for a stably-stratified IS
233 would likely be warmer than that observed at $z = -2.7$ m. By 0800 h, the SZ was rapidly warm-
234 ing from solar radiation, whereas the IS temperature dropped as the DIT approached its maximum
235 cold phase at approximately 1000 h. Thus, alongshore gradients were weak relative to the 0.5 °C
236 cross-shore difference.

b. General Tracer Observations

237 By 1020 h ($t_r = 5.02$ h), the beginning of the deformation period, the dye plume extended
238 approximately 4 km alongshore (Fig. 5a). The northern portion of the dye plume ($y > 2.5$ km,
239 denoted SZ-plume) was narrow (< 200 m, or $< 2L_{sz}$) and shoreline attached with northward
240 tracer transport over the day (Fig. 5a-c), consistent with SZ currents driven by obliquely incident
241 south-swell (Longuet-Higgins 1970a,b). In contrast, at the same time the southern portion of the
242 plume ($y < 2$ km, hereafter the IS-plume) was up to 800 m (or $8L_{sz}$) wide, extending into almost
243 $h = 12$ m depth and was shoreline detached to the south ($y < 400$ m). This implies that some
244 transport mechanism brought the SZ released tracer out to $8L_{sz}$ over 3-5 h. Between 1020 h and
245 1230 h (denoted deformation period, gray bar in Fig. 3 and 4) tracer in the IS-plume deformed
246 onshore to $5L_{sz}$ and was transported south, while a dye free SZ intrusion advected from the south,
247 further detaching the IS-plume from the shoreline (Fig. 5a-c). The northward advection of the
248 SZ-plume and the southward advection of the IS-plume resulted in a 9 km alongshore extent by

249 1658 h ($t_r = 11.65$ h). At this time (≈ 6.5 h after the deformation period ended), the plume still
250 remained within $8L_{sz}$ from shore at the surface (Fig. 5d). Here, we focus on the deformation period
251 evolution of the IS-plume.

c. Deformation Period Large-Scale Inner-Shelf Plume Evolution

252 During the deformation period (gray bar in Fig. 3), the offshore plume boundary (thick black
253 $\bar{D} = 1$ ppb contour in Fig. 6) propagated onshore at up to 5 cm s^{-1} , deforming the plume. Con-
254 currently, the IS-plume elongated alongshore with the southern front moving past the release point
255 at approximately 7 cm s^{-1} . Meanwhile, a dye free region within the SZ moved north at a similar
256 rate, detaching the IS-plume from shore (dark gray in Fig. 6).

FIG. 7

257 The large-scale vertical and cross-shore structure of the IS temperature and plume deformation
258 can be seen along the AUV transect ($y = 395$, dashed red line in Fig. 6). Toward the beginning
259 of the deformation period at 1049 h (first red bar, Fig. 4c), the IS-plume was surface trapped
260 ($\tilde{z} \geq -3$ m) and extended offshore of $\tilde{x} = -700$ m (Fig. 7a), with isotherms sloping upward
261 toward shore (e.g., $\bar{T} = 20.5$ °C isotherm slope, dashed in Fig. 7c). At this time, the SZ temperature
262 was ≈ 21.75 °C, about 0.25 °C greater than the maximum observed AUV temperature, indicating
263 that the isotherm slope changed sign between the SZ and $\tilde{x} = -400$ m (or $\approx 4L_{sz}$). Additionally,
264 the dye plume was largely confined to $T \geq 20.25$ °C, about 0.45 °C below the minimum of T_{rel}
265 (magenta, Fig. 4c), indicating mixing with colder water prior to the deformation period.

FIG. 8

266 Consistent with the aerial dye observations (Fig. 6), later in the deformation period at 1151 h
267 (second red bar, Fig. 4c), the offshore dye front moved onshore to $\tilde{x} \approx -500$ m (Fig. 7b) and
268 deepened ($\tilde{z} \geq -6$ m). At this time, the AUV $\bar{T} = 20.5$ °C isotherm deepened, consistent with the

269 deepening Tr isotherms (dashed line below gray bar in Fig. 4a) and the isotherm slope changed sign
270 (sloping upward offshore). The deepening AUV isotherms and dye plume suggest that the cross-
271 shore plume narrowing was partially balanced by vertical thickening. The observed relaxation of
272 the cross-shore temperature gradient over the deformation period is also consistent with baroclinic
273 flow associated with the DIT (Fig. 4b).

274 Deformation period warming and IS-plume deepening were also observed along TA transect
275 ($\tilde{x} \approx -350$ m and $h \approx 6.5$ m, cyan in Figs. 1 and 6), which captures both alongshore and temporal
276 variations in the large-scale temperature and dye fields. Between 1107 h and 1208 h (cyan bar,
277 Fig. 4c; and $0.54 \lesssim y \lesssim 2.7$ km, Fig. 8) the TA temperature increased with time (or y) at all
278 depths, with the greatest increase of ≈ 1 °C below $\tilde{z} = -5$ m. The isotherms sloped downward
279 roughly 1.2 m km⁻¹ or 2.82 m h⁻¹ relative to space or time, respectively.

280 The TA dye plume deepened at a rate similar to the isotherms and eventually detached from
281 the surface (Fig. 8b). Initially, at $y = 0.54$ km (1107 h) the dye was confined to $\tilde{z} > -4$ m
282 (Fig. 8b) and the $\bar{T} = 20.5$ °C isotherm was at roughly $\tilde{z} = -4.5$ m. The dye reached $\tilde{z} = -6$ m
283 by about $y = 0.8$ km (or 1115 h), and by $y = 1.5$ km dye was capped by a warmer $\mathcal{O}(21.5$ °C)
284 layer. The dye then remained subsurface as the TA extended north, beyond the IS-plume region
285 (*i.e.*, $y > 2$ km). Similar to AUV, the dye was largely confined to $20.25 \leq \bar{T} \leq 21.5$ °C as both
286 isotherms and iso-dye deepened.

d. Release & Deformation Period Statistical Plume Evolution

287 To examine temporal evolution of joint (D, T) statistics and evaluate the role of mixing in
288 observed IS-plume evolution, arithmetic temperature and logarithmic dye means and standard de-

289 viations were calculated over 3-4 approximately 44 min time intervals from all raw (*i.e.*, unfiltered
290 and not interpolated) SZ, AUV, and TA observations where $D \geq 1$ ppb. The average SZ-plume
291 (predominantly from instruments S2-S3 & M1-M4 in Fig. 1) temperature increased > 1 °C from
292 0942–1154 h due to solar heating. The standard deviation of SZ-plume temperature also increased
293 with time from approximately 0.1-0.25 °C (horizontal black dotted lines, Fig. 9) due to an increase
294 in SZ temperature anomalies during the deformation period (gray shading, Fig. 4c). Meanwhile,
295 average SZ dye concentration decreased by an order of magnitude, with the standard deviation
296 in concentration (vertical black dotted lines, Fig. 9) increasing. The large standard deviation in
297 SZ-plume dye concentration at $t = 1025$ h was due to an ≈ 30 ppb concentration difference be-
298 tween instruments M1 & M2 and instruments S2, S3 & M3 (see Fig. 1b). The SZ-plume joint
299 dye/temperature evolution indicates a fast response to solar forcing and vigorous lateral mixing.

300 In contrast, the IS-plume joint dye and temperature statistics were relatively stable in time.
301 The average observed temperature of the IS-dye plume increased slightly (≈ 0.25 °C) during the
302 deformation period (Fig. 9), less than half that of the SZ-plume, consistent with a depth depen-
303 dent response to solar heating. The standard deviation of temperature in the IS-plume (*i.e.*, at both
304 TA and AUV) remained roughly 0.25 °C throughout the deformation. The IS-plume dye concen-
305 tration was much lower than the SZ and did not decrease considerably over the morning, varying
306 between 2.5–6 ppb, with a standard deviation around 1.8 ppb (red and blue vertical dotted lines
307 in Fig. 9). The broader $t = 0942$ h temperature distribution on the IS illustrates that the IS-plume
308 was vertically stratified prior to deformation. The consistent IS-plume temperature span and dye
309 concentration suggests vertical mixing was not responsible for the observed IS-plume deepening
310 during the deformation period.

FIG. 10

e. Large-scale Cross-shore Convergence & Alongshore Elongation of Inner-Shelf Plume

311 The deformation period MASS surface dye and temperature measurements suggest that the
312 IS-plume narrowing and elongation (Fig. 6) was largely driven by advection. Here measurements
313 are examined on a cross-shore line at $y = 818$ m within the IS-plume (gray dashed line Fig. 6).
314 Prior to deformation at 1020 h, the offshore $\bar{D} = 1$ ppb contour (Fig. 6a) was roughly 700 m from
315 shore on the MASS cross-shore line. At this time, there was an IS surface temperature gradient
316 $\partial\bar{T}/\partial\tilde{x}$ (calculated between $\tilde{x} = -800$ and -100 m) of -0.38 °C km⁻¹ (*i.e.*, colder onshore,
317 lower black curve, Fig. 10b). Between 1020 and 1137 h the $\bar{D} = 1$ ppb front (red dashed line,
318 Fig. 10a) moved on-shore about 275 m, and remained < 500 m offshore until 1217 h (lower yel-
319 low curve, Fig. 10a). The onshore speed u_f was approximately 5 cm s⁻¹ and was estimated as,
320 $u_f = \Delta x_f/\Delta t + v(\delta x_f/\delta y_f)$, where $\Delta x_f/\Delta t$ is the shore-ward progression of the $\bar{D} = 1$ ppb
321 contour along the MASS line and $v(\delta x_f/\delta y_f)$ accounts for the southward advection of the sloped
322 contour where it intersects the MASS line. Meanwhile, the MASS cross-shore temperature gra-
323 dient continuously increased, switching sign, and reaching approximately 0.2 °C km⁻¹ at 1217 h,
324 consistent with the relaxation of shoaled isotherms observed at Tr (Fig. 4a) and the reversal of the
325 cross-shore temperature gradient at AUV (Fig. 7c-d).

326 In contrast to the onshore progression of the $\bar{D} = 1$ ppb contour, between 1020 h and 1036 h
327 the cross-shore location of the peak dye concentration \bar{D}_{\max} (blue dashed Fig. 10a) moved offshore
328 ≈ 100 m to $\tilde{x} \approx -250$ m, as the dye-free intrusion progressed north in the SZ and crossed
329 the MASS transect (see Fig. 6a-b). The dye maximum then moved onshore ≈ 60 m at roughly
330 1 cm s⁻¹. Additionally, the \bar{D}_{\max} decrease in time was relatively small. As such, the average
331 $\partial\bar{D}/\partial\tilde{x}$, calculated as the slope of $\bar{D}(x)$ between $\bar{D} = 1$ ppb and \bar{D}_{\max} (*i.e.*, red and blue curves

332 in Fig. 10a), increased from 28 ppb km⁻¹ at 1020 h to 66 ppb km⁻¹ at 1137 h (not shown). The
333 steepening offshore dye gradient indicates convergent onshore advection (consistent with the DIT)
334 as opposed to a diffusive advancement of the $\bar{D} = 1$ ppb contour, which would require an up-
335 gradient diffusive flux and an inferred negative cross-shore diffusivity between $-8 \text{ m}^2 \text{ s}^{-1}$ and
336 $-2 \text{ m}^2 \text{ s}^{-1}$. Thus, shoreward advancement of the $\bar{D} = 1$ ppb contour was largely due to advection. FIG. 11

337 Coincident with the cross-shore deformation, the IS-plume elongated (strained) in the along-
338 shore direction (Figs. 6 & 7). This elongation is also evident in the alongshore y evolution of the
339 cross-shore maximum dye concentration $\bar{D}_{\max}(y)$ (Fig. 11). At 1020 h (black curve, Fig. 11) the
340 southern edge of the IS-plume was just north of the release location ($y = 0$ in Figs. 6 & 11) and
341 farther to the north there were several prominent ≈ 5 ppb magnitude and ≈ 250 m wide features
342 (*e.g.*, tail of arrows in Fig. 11). Between 1020 h and 1217 h the southern dye front advected south-
343 ward at $\approx 6.5 \text{ cm s}^{-1}$, approaching $y = -500$ m (left arrow, Fig. 11). Coherent D_{\max} features at
344 $y \leq 750$ m also propagated to the south at $\approx 1.5 \text{ cm s}^{-1}$ (middle arrow, Fig. 11). At $y \approx 1.5$ km,
345 features advected northward at $\approx 3 \text{ cm s}^{-1}$ (right arrow, Fig. 11). The differential advection of
346 plume features implies an average alongshore plume straining of $4.5 \text{ cm s}^{-1} \text{ km}^{-1}$.

347 The IS-plume centerline (cross-shore position of \bar{D}_{\max}) was tilted slightly from shore paral-
348 lel south of MASS transect (Fig. 6), resulting in some aliasing of cross-shore sheared alongshore
349 transport into observed elongation. The bathymetry also varies slightly alongshore (Fig. 6). How-
350 ever, the alongshore elongation apparent in D_{\max} (Fig. 11) is also apparent using \bar{D} at a fixed
351 cross-shore distance (*e.g.*, 200-400 m) or along a given bathymetry contour (*e.g.*, 4-8 m), yielding
352 similar strain rates. This suggests that potential aliasing due to cross-shore plume structure was
353 weak. During the deformation period, the IS-plume centerline tilt (relative to the shoreline) south
354 of the MASS transect decreased from 0.15 to 0.05 (not shown) predominantly due to the onshore

355 advection of \bar{D}_{\max} , rather than due to the southward propagating front. Combined with the pres-
356 ence of straining between \bar{D}_{\max} features north of MASS transect ($y > 800$ m, Fig 11), where the
357 centerline was nearly shore parallel, indicates that the alongshore plume elongation was not driven
358 by alongshore uniform shear, *i.e.*, $\partial v/\partial x$.

f. Small-Scale and High-Frequency Inner-Shelf Plume Evolution

FIG. 12

359 In addition to large-scale dye \bar{D} and temperature \bar{T} , the small-scale D' and T' fields had
360 rich structure and evolution (*e.g.*, D' in Fig. 2c). At mooring Tr, high frequency (HF, see Sec-
361 tion 2d) temperature fluctuations were approximately ± 0.25 °C with timescales of roughly 10 min
362 (Fig. 12), longer than the depth- and time-averaged buoyancy period of roughly 4.5 min. HF IW
363 fluctuations with similar timescale were observed at ADCP with u' magnitude of ≈ 1 cm s⁻¹ (not
364 shown).

365 The T' fluctuations were near-surface intensified (*i.e.*, the maximum $T'(z)$ was at $z \geq -6$ m)
366 just prior to and throughout the deformation period, coincident with the maximum of the DIT
367 cold phase (Fig. 12). Largest T' fluctuations occurred near the depth of the maximum 3 h large-
368 scale filtered vertical temperature gradient (dotted line in Fig. 12) as expected from WKB theory
369 (*e.g.*, Hendershott 1981), indicating that the large-scale DIT modulated the vertical structure of the
370 HF IWs, potentially enabling HF IWs to propagate into shallower water and contribute to nearshore
371 mixing and exchange. HF IWs are often linked to internal tide (*e.g.*, Zhang et al. 2015).

FIG. 13

372 The signature of HF IWs are also evident in small scale surface temperature and dye fields
373 (Fig. 13). HF IWs have been observed previously via aerial LWIR (*e.g.*, Walsh et al. 1998; Mar-
374 morino et al. 2004) with the surface T' signal attributed to IW modulation of the surface thermal

375 layer (Farrar et al. 2007). The surface IW dye signal is likely the result of IW horizontal conver-
 376 gence (divergence) that thickened (thinned) the near-surface plume, slightly altering the remotely
 377 sensed concentration (*e.g.*, Fig. 2c). The cross-shore gradient ($\partial D'/\partial x$ and $\partial T'/\partial x$) further high-
 378 lights the small-scale features (Fig. 13). For example, at $t = 1155$ h, a packet of HF IW intersected
 379 the MASS transect (gray dashed line in Fig. 13) at $\tilde{x} \approx -200$ m and within the IS-plume. The
 380 packet was roughly alongshore oriented and extended between $200 \lesssim y \lesssim 1500$ m in $\partial T'/\partial x$
 381 (Fig. 13b). This feature is also present in the $\partial D'/\partial x$ field for $500 < y < 1500$ m (Fig. 13a).
 382 Other, somewhat weaker, small-scale $\partial T'/\partial x$ features are present outside the plume, but not in the
 383 $\partial D'/\partial x$ field as $D = 0$. Onshore of $\tilde{x} = -250$ m, the signature of rip-currents are also present in
 384 D' and T' , where features have significantly shorter (≈ 100 m) alongshore length scales.

FIG. 14

385 During the deformation period, HF IWs with a cross-shore length-scale $\lambda_{iw} \approx 60$ m propagated
 386 shoreward through the IS-plume, as evidenced in the small-scale $\partial D'/\partial \tilde{x}$ and $\partial T'/\partial \tilde{x}$ Hovmöller
 387 plots (Fig. 14). The HF IW packet at $\tilde{x} \approx -200$ m in Fig. 13 entered the IS-plume along the
 388 MASS transect at $t \approx 1040$ h and $\tilde{x} \approx -700$ m (start of dashed line in Fig. 14a). The packet
 389 propagated shoreward at roughly 9 cm s^{-1} to $\tilde{x} \approx -400$ m where a steeper trailing front developed
 390 (red and blue banding in Fig. 14b), consistent with wave steepening, and it rapidly decelerated
 391 onshore of $\tilde{x} \approx -300$ m. Several similar features intersected the MASS transect (onshore of
 392 TA and AUV) during the deformation period, each separated by approximately 30-45 min (*e.g.*, the
 393 front that passed $\tilde{x} = -500$ m at $t = 1030$ h in Fig. 14).

394 The steepening and deceleration of the surface features is qualitatively consistent with weakly
 395 nonlinear eKdV solutions on a slope (*e.g.*, Holloway et al. 1999). IW transformation (*i.e.*, steepen-
 396 ing, and breaking) primarily results from changes in depth (*e.g.*, Sutherland et al. 2013) or
 397 stratification (*e.g.*, Grimshaw et al. 2004). Both mechanisms are possible as HF IW approach the

398 SZ, where $h \rightarrow h_{sz}$ (h_{sz} is the depth of the outer-SZ) and $N \rightarrow 0$.

399 Onshore of $\tilde{x} = -300$ m, the coherence between the HF IW D' and T' signals decreases.
400 The fade in D' HF IW signal is partially due to aliasing near \bar{D}_{\max} between $\tilde{x} = -300$ m and $\tilde{x} =$
401 -200 m. Based on movies of small-scale dye and temperature fields, SZ generated TRCs were also
402 active close to shore ($\tilde{x} \geq -250$ m $\approx -2.5L_{sz}$, not shown). The TRC variability may be partially
403 responsible for the decoherence of the propagating D' and T' fronts onshore of $\tilde{x} = -250$ m in
404 Fig. 14. The eventual disintegration of the HF IW T' signals before reaching the SZ/IS boundary
405 ($\tilde{x} = -L_{sz} \approx -100$ m) suggests there is IW dissipation in the region $-400 \leq \tilde{x} \leq -100$ m.
406 HF IW dissipation has been linked to vertical mixing on the shelf (e.g., Walter et al. 2012), thus
407 mixing may be enhanced in the region onshore of AUV and TA transects where IS-plume (D, T)
408 statistics were stable. However, in the near-SZ region where surface HF IW signatures disappear,
FIG. 15 NLIW can still propagate to SZ as near bed cold bores (Sinnott et al. 2018).

410 The LWIR-observed HF IW activity was not alongshore uniform over the study region. The
411 temporal $\text{rms}(\partial T'/\partial x)$ between 1020-1230 h was elevated on the IS in the region offshore of
412 $0.5 \leq y \leq 2.5$ km, with magnitudes ≥ 1 °C km⁻¹ or ≈ 2 –3 times greater than to north and south
413 (Fig. 15). The persistent small-scale gradients in this region are attributed to the HF IWs shown
414 in Figs. 13 & 14, whereas the elevated signal onshore of roughly $2.5L_{sz}$ was due to TRC activity.
415 The alongshore extent of the enhanced IS $\text{rms}(\partial T'/\partial x)$ bounds the region of IS-plume elongation
416 (Fig. 11), suggesting that either incident HF IWs were intensified in this region or this was where
417 the DIT shoaled the high N^2 region (e.g., Fig. 12). The former implies HF IW mass-transport or
418 momentum-flux driven plume elongation, whereas the latter implicates the DIT, these mechanisms
419 are discussed in Section 4c.

4. Discussion

a. Summary of Results

420 The 3.84 h early morning dye release evolved for ≈ 5 h before intensive IS *in situ* and aerial
421 remote observations began. Prior to deformation, the IS-plume was advected up to $8L_{sz}$ (800 m)
422 offshore and was confined to the surface, with tracer above $\tilde{z} = -3$ m for $\tilde{x} \leq -400$ m (Fig. 7a).
423 As aerial observations began, the IS tracer plume was observed deforming shoreward, elongating
424 in the alongshore and being transported south, while SZ tracer was continuously transported north-
425 ward (Fig. 5a-d). Large-scale Tr temperature and ADCP cross-shore velocity (Fig. 4a-b) indicate
426 that the early morning offshore dye transport and mid-late morning deformation occurred during
427 two phases of the DIT.

428 Over the deformation period, the offshore IS plume $\bar{D} = 1$ ppb front propagated onshore
429 at roughly 5 cm s^{-1} as the IS-plume and its associated isotherms deepened at $\tilde{x} \approx -4L_{sz}$ along
430 AUV (Figs. 4 and 7). The steepening offshore dye gradient indicates that onshore progression of
431 the IS-plume was due to advection. Similarly, the IS-plume joint dye and temperature distribution
432 was relatively stable offshore of $\tilde{x} = -4L_{sz}$, indicating that the IS-plume deepening was not
433 predominantly due to vertical mixing.

434 During the deformation period, surface intensified HF IW (≈ 10 min period) were observed
435 at mooring Tr (Fig. 12). These HF IW propagated onshore and through the IS-plume at roughly
436 9 cm s^{-1} for $\tilde{x} \leq -3L_{sz}$, then decelerated in shallower water, breaking up into multiple IWs and
437 presumably steepening (Figs. 13 & 14). The HF IW variance was enhanced in the 2 km alongshore
438 region of the IS-plume deformation and elongation, and was much weaker just to the north and

439 south (Fig. 15).

b. Mechanism of IS-Plume Deepening

440 The IS isotherm and plume deepening observed by AUV, TA, and Tr during the deforma-
441 tion period could result from cross-shelf exchange flow or alongshore advection of an alongshore
442 temperature and plume gradient, or a combination of the two. The DIT had both a cross-shore
443 exchange structure (Fig. 4a-b) and (north-to-south) alongshore phase propagation (Fig. 3d), indi-
444 cating the presence of an IS alongshore temperature gradient during the release and deformation
445 periods. Here, an idealized two layer cross-shelf exchange model is used to examine whether the
446 observed plume deepening can be due to surface onshore flow associated with the DIT relaxation.

447 By continuity and assuming alongshore uniformity, a two layer cross-shore exchange flow, with
448 onshore flow at the surface and compensating offshore flow at depth, drives interface deepening.
449 At a given cross-shore location x_0 , onshore transport within the surface layer is balanced by an
450 increase in (x, z) cross-sectional area A of the surface layer onshore of x_0 , *i.e.*,

$$u_s H = \partial A / \partial t, \quad (2)$$

451 where u_s is the average surface velocity and $H(t)$ is the cross-shore uniform surface layer depth.
452 As the IS-plume remained offshore of the SZ during the deformation (Fig. 6), the approximate area
453 onshore of AUV (*i.e.*, with $x_0 = -400$ m) is,

$$A = H L_x - (H - h_{sz})^2 (2\beta)^{-1}, \quad (3)$$

454 where $L_x = -(x_0 + L_{sz})$, $L_{sz} \approx 100$ m is the SZ width, and $h_{sz} \approx 2$ m is the depth at $\tilde{x} = -L_{sz}$, and
455 $\beta = 0.017$ is the constant bathymetric slope. Substituting (3) into (2) and integrating (assuming

456 constant u_s) gives, $u_s \approx \Delta t^{-1}[(L_x + h_{sz}\beta^{-1}) \ln(H_f/H_i) - \beta^{-1}\Delta H]$, relating the surface layer
457 deepening $\Delta H = H_f - H_i$ to the exchange velocity u_s . Based on the observed plume deepening at
458 AUV (initial $H_i = 3$ m and final $H_f = 6$ m at $\tilde{x} = -400$ m over $\Delta t \approx 3720$ s, Fig. 7a-b), the two
459 layer exchange model implies a u_s of ≈ 3 cm s⁻¹. This velocity estimate is consistent with both
460 the 5 cm s⁻¹ onshore progression of the $\bar{D} = 1$ ppb front observed along MASS (Fig. 10a) and
461 is of similar magnitude to the observed large-scale DIT cross-shore velocities below $z = -5$ m at
462 ADCP (Fig. 4b).

463 Alternatively, southward advection of an alongshore gradient can appear as local temporal evo-
464 lution (*i.e.*, $\partial H/\partial t \sim -\bar{v}\partial H/\partial y$, where \bar{v} is the depth averaged alongshore current). Taking the
465 observed deepening along TA, $\partial H/\partial y \approx 1.2$ m km⁻¹, and using the southward plume front veloc-
466 ity ($|\bar{v}| < 10$ cm s⁻¹), gives a maximum of $\partial H/\partial t \approx 0.43$ m h⁻¹ or roughly 25% of the observed
467 deepening at AUV. Additionally, the phase propagation of the DIT from the mooring array was
468 much greater than the observed alongshore currents. Thus, the observed plume deepening and
469 deformation was likely due to a cross-shore exchange flow associated with the DIT.

c. Mechanisms for IS-Plume Elongation

470 The IS-plume elongation (Fig. 11) suggests a near-surface alongshore straining $\partial v_s/\partial y$ of
471 roughly 4.5 cm s⁻¹ km⁻¹. The presence of both northward and southward propagating features
472 in Fig. 11 indicates that the straining may be localized to the ≈ 2 km IS-plume elongation re-
473 gion ($0 \leq y \leq 2$ km), which overlaps the region of elevated HF IW surface rms($\partial T'/\partial x$)
474 ($0.5 \leq y \leq 2.5$ km), suggesting there may be a relationship between the large-scale alongshore
475 strain (elongation) and the IS HF IW alongshore inhomogeneity (Fig. 15).

476 An imbalance in the large-scale cross-shore 2-layer DIT exchange flow due to excess onshore
477 surface flow in the elongation region, *i.e.*, $u_s(y)$, can support an alongshore strain. Assuming
478 the cross-shore convergence occurs over $L_x \approx 500$ m (the approximate cross-shore width of the
479 IS-plume), an excess onshore $u_s \approx 2.25 \text{ cm s}^{-1}$ is sufficient to support the observed straining.
480 This implies a DIT $u_s \approx 5.25 \text{ cm s}^{-1}$ in the elongation region, slightly larger than the onshore
481 progression of the $\bar{D} = 1$ ppb front. This would also require the DIT to have a relatively short
482 ≈ 4 km alongshore length scale, either due to direction of propagation or alongshore gradients
483 induced by the geometry of the San Diego Bight.

484 HF IWs can drive cross-shore mass transport. A single non-dissipative internal solitary wave
485 induces horizontal mass displacement that increases with non-linearity, represented by the ratio of
486 IW fluid velocity u_{iw} to wave celerity c , and with wave-length (*i.e.*, u_{iw}/c and λ_{iw} , *e.g.*, Lamb
487 1997). Based on observed IW characteristics ($u_{iw}/c \approx 0.11$ and $\lambda_{iw} \approx 60$ m), the individual
488 solitary IW surface displacement was potentially $\mathcal{O}(1.5 \text{ m})$ (Lamb 1997, Eq. A8). In a wave
489 averaged sense, incremental solitary wave displacements lead to mass transport (*e.g.*, Shroyer
490 et al. 2010; Zhang et al. 2015), analogous to surface gravity wave Stokes drift (Henderson 2016).
491 Over the deformation period the HF IWs potentially account for a net onshore displacement of
492 roughly 15 m (*i.e.*, passage of 10 waves), or an IW induced $u_s \approx 0.2 \text{ cm s}^{-1}$. Thus, internal
493 solitary wave Stokes drift was insufficient to support the observed elongation.

494 In addition to IW Stokes drift, IWs also have a momentum flux, akin to a radiation stress.
495 Wave-dissipation induced divergence of IW momentum flux generates cross-shore pressure gradi-
496 ents (*e.g.*, Wunsch 1971; Suanda et al. 2017) and, for obliquely incident IWs, alongshore currents
497 (*e.g.*, Thorpe 1999; Zikanov and Slinn 2001). In the region $-4L_{sz} \geq \tilde{x} \geq -2.5L_{sz}$, observed HF
498 IWs appear to steepen and dissipate (Fig. 14) and HF IW activity was concentrated in the elon-

499 gation region (Fig. 15). In analogy to alongshore gradients in surface gravity wave height (and
500 radiation-stress) generating alongshore SZ pressure gradients and circulation cells (Bowen 1969),
501 an elevated IW energy flux and dissipation in the region of the IS-plume might create a baro-
502 clinic pressure driven alongshore elongation. In the context of IWs incident on near-critical slopes,
503 breaking and along-slope flow is generated near the bottom or within a critical layer (*e.g.*, Zikanov
504 and Slinn 2001), and thus are not likely to cause near-surface currents. However, in the present
505 case of HF low-mode or solitary-like waves dissipating near shore, the vertical structure or velocity
506 scale is unclear.

507 As the DIT was responsible for the observed large-scale cross-shore exchange flow, and the
508 magnitude of the exchange velocity (inferred from velocities below $z < -5$ m) were of similar
509 magnitude as needed to support both deepening and straining, the DIT was therefore also likely
510 responsible for the IS-plume alongshore elongation. While other possible mechanisms can induce
511 strain, they were not consistent with observations. Although, a contribution from HF IW momen-
512 tum flux cannot, at present, be discounted. In either case (DIT or HF IW momentum flux), this
513 implies an inhomogeneity of the DIT over the fairly narrow alongshore elongation region. If the
514 HF IWs were generated through an instability of the DIT, then spatial patterns of the DIT would
515 subsequently be reflected in the HF IW field, hence the patterns in Fig. 15.

d. Influence of Tracer Release Timing

516 Previous SZ dye release experiments released from mid- to late morning and observed along-
517 shore SZ transport over several km and dye confined to within $2L_{SZ}$ - $3L_{SZ}$ (*e.g.*, Grant et al. 2005;
518 Clark et al. 2010; Hally-Rosendahl et al. 2015). These three dye releases took place in Southern

519 California in May, September, or October when solar forcing was strong. A mid-day tidal inlet dye
520 release during strong obliquely incident waves and alongshore wind, had dye transported along-
521 shore in the SZ for about 9 km and also largely confined $2L_{sz}$ - $3L_{sz}$ (Feddersen et al. 2016). The
522 observed SZ-IS temperature difference was ≈ 1 °C, due to warm dye-laden ebb tidal-inlet water
523 in the SZ. In contrast, following R2, dye was observed out to $\tilde{x} = -8L_{sz}$, and the subsequent
524 IS-plume shoreward deformation and late morning to afternoon southward transport (Fig. 5), is in
525 stark contrast to the more canonical SZ-plume towards the north ($y \geq 3$ km, Fig. 5). Here, the
526 influence of the early morning release timing (0518-0908 h) relative to the DIT and solar cycle is
527 examined.

528 Tracer release began when the SZ was colder than the surface-IS (*i.e.*, $t < 0800$ h, Fig. 4c).
529 As such, tracer exchanged onto the IS prior to 0800 h would have been expected to preferentially
530 spread offshore at depth, largely following the tracer release isotherm (*i.e.*, weak mixing). In a
531 modeling study of TRC SZ-IS exchange without solar forcing, SZ released tracer was transported
532 offshore in an IS sub-surface layer due to the interaction of TRCs and IS stratification (Kumar
533 and Feddersen 2017b). However, despite the SZ being colder than the near-surface IS during
534 much of the release, the IS plume was surface intensified because the DIT drew even colder water
535 onshore at depth preventing IS-plume subduction. If the DIT had not occurred, the IS-plume may
536 have remained closer to shore with subduction of the dye maximum, as observed farther north at
537 $y = 2.5$ km near the boundary between SZ and IS plumes (Fig. 8).

538 In addition to influencing the vertical structure and cross-shore extent of the IS-plume during
539 the release period, the DIT also modulated the IS-plume thermal evolution. Hally-Rosendahl et al.
540 (2014) observed a SZ and IS (D, T) distribution, with higher average SZ dye and temperature and
541 stronger IS stratification. Here, a similar (D, T) relationship was observed prior to the deformation

542 period (circles, Fig. 9), although with some differences. The Hally-Rosendahl et al. (2014) dye was
543 released in $T > 19\text{ }^{\circ}\text{C}$ and was diapycnally mixed to $T = 18\text{ }^{\circ}\text{C}$ on the IS within $2L_{\text{SZ}}$. Here, the IS-
544 plume tracer was quasi-adiabatically advected to a depth of 6 m at $4L_{\text{SZ}}-6L_{\text{SZ}}$ with cross-isotherm
545 dye mixing limited to $\leq 0.5\text{ }^{\circ}\text{C}$.

546 Additionally, the mid-late morning increase in SZ-IS plume temperature separation (Fig. 9)
547 resulted from the early morning cross-shore plume advection (*i.e.*, the $8L_{\text{SZ}}$ cross-shore extent),
548 and a reduced solar heating in deeper water. As such, by the end of the deformation period, the SZ
549 and IS plumes had a $\approx 1\text{ }^{\circ}\text{C}$ mean temperature difference even though they had similar mean dye
550 concentration (Fig. 9). Subsequently, during and after deformation, the warmer SZ may have been
551 a thermal barrier for the IS-plume. Omand et al. (2011) argued a similar mechanism prevented an
552 IS phytoplankton bloom from reaching the warm SZ following a large IW upwelling event.

553 Shoreline-released tracer released at alternate phases of either the internal tide or the solar
554 cycle would be expected to evolve differently. In particular, tracer released during the deformation
555 period (warm surfzone) would likely not have formed the IS-plume and the overall alongshore
556 plume extent would have largely followed the northward SZ currents. Alternatively, if tracer had
557 been released even earlier in the DIT cooling phase (*i.e.*, around mid-night) with SZ colder than
558 near-surface IS, even more tracer may have been advected onto the IS with subsequent southward
559 advection over the deformation and elongation period. Thus, release timing relative to the solar
560 cycle and any internal tide events is relevant to the transport and dispersion of shoreline-released
561 tracers (*e.g.*, human pathogens, or larvae) to the IS and also likely for the IS to the SZ.

5. Summary & Conclusions

562 An early-morning SZ tracer release coinciding with the cooling phase of the DIT resulted in, an
563 anomalously large (relative to previously observed SZ dye release experiments) $8L_{SZ}$ cross-shore
564 plume width after 3-5 h, extending well onto the IS. During the subsequent DIT warming phase
565 (next ≈ 2 h), this IS-plume deformed (narrowed) cross-shore to $5L_{SZ}$, vertically thickened by up
566 to 3 m, and strained (elongated) alongshore, yet remained offshore of the SZ. This large-scale
567 IS-plume evolution is consistent with a simple 2-layer cross-shore exchange model.

568 The DIT-augmented cross-shore tracer transport also coincided with the transition from night-
569 time cooling to solar heating. The shallow SZ warmed more rapidly than the near-surface IS, induc-
570 ing separate SZ- and IS-plume T evolution. The development of a positive cross-shore temperature
571 gradient may have blocked the IS-plume from entering the SZ. Additionally, a DIT alongshore
572 gradient (over ≈ 2 km) could support the observed IS-plume elongation. Small-scale processes,
573 *e.g.*, TRC and HF IW, interacted with the IS-plume, likely contributing to vertical mixing onshore
574 of $4L_{SZ}$ and SZ-IS exchange. Coupled with opposing SZ/IS alongshore currents, the release timing
575 relative to both the DIT and solar cycle resulted in the ≈ 9 km alongshore plume extent in roughly
576 12 h (*i.e.*, SZ-plume ≈ 7 km north of release and IS-plume ≈ 2 km south of the release).

577 These observations demonstrate that nearshore tracer exchange is influenced by both SZ and IS
578 processes spanning a broad range of scales. Here, we have shown that the interaction and relative
579 phasing of the DIT with solar warming can have a significant effect on the evolution of shoreline
580 released tracer over ≈ 5 -12 h.

581 *Acknowledgments.* Thanks to two anonymous reviewers who greatly helped improve this
582 manuscript. This work was funded under the CSIDE grant by the National Science Foundation
583 (NSF OCE-1459389), and through the NSF Graduate Research Fellowship Program. Data was

584 made available in part by SIO CDIP, and the Tijuana River National Estuary Research Reserve and
585 are available through the CSIDE web-page (<https://scripps.ucsd.edu/projects/cside/>) or by contact-
586 ing the corresponding author. The U.S. Navy provided access to Navy property for data collec-
587 tion. We thank Ken Melville, Luc Lenain, Nick Statom, and Stephen Holleman for acquisition
588 and preliminary processing of MASS data. We thank YMCA: Camp Surf for providing a base
589 of operations; the cities of Imperial Beach and Coronado, the US Navy and CA State Parks for
590 accommodating our research activities; and the numerous Imperial Beach lifeguards, UCSD/SIO
591 students, and volunteers for efforts to keep beachgoers safe and monitor surfzone instrumentation.

REFERENCES

592

- 593 Austin, J. A., and S. J. Lentz, 2002: The inner shelf response to wind-driven up-
 594 welling and downwelling. *Journal of Physical Oceanography*, **32**, doi:10.1175/1520-
 595 0485(2002)032<2171:TISRTW>2.0.CO;2, 2171–2193.
- 596 Barbier, E. B., S. D. Hacker, C. Kennedy, E. W. Koch, A. C. Stier, and B. R. Silliman, 2011: The
 597 value of estuarine and coastal ecosystem services. *Ecological Monographs*, **81**, doi:10.1890/10-
 598 1510.1, 169–193.
- 599 Bowen, A. J., 1969: Rip currents: 1. theoretical investigations. *Journal of Geophysical Research*,
 600 **74**, doi:10.1029/JC074i023p05467, 5467–5478.
- 601 Brown, J., J. MacMahan, A. Reniers, and E. Thornton, 2009: Surf zone diffusivity on a rip-
 602 channeled beach. *Journal of Geophysical Research: Oceans*, **114**, doi:10.1029/2008JC005158.
- 603 Brown, J. A., J. H. MacMahan, A. J. H. M. Reniers, and E. B. Thornton, 2015: Field observations
 604 of surf zone-inner shelf exchange on a rip-channeled beach. *Journal of Physical Oceanography*,
 605 **45**, doi:10.1175/JPO-D-14-0118.1, 2339–2355.
- 606 Clark, D. B., S. Elgar, and B. Raubenheimer, 2012: Vorticity generation by short-crested wave
 607 breaking. *Geophysical Research Letters*, **39**, doi:10.1029/2012GL054034.
- 608 Clark, D. B., F. Feddersen, and R. T. Guza, 2010: Cross-shore surfzone tracer dis-
 609 persion in an alongshore current. *Journal of Geophysical Research: Oceans*, **115**,
 610 doi:10.1029/2009JC005683, n/a–n/a, c10035.
- 611 Clark, D. B., L. Lenain, F. Feddersen, E. Boss, and R. T. Guza, 2014: Aerial imaging of
 612 fluorescent dye in the near shore. *Journal of Atmospheric and Oceanic Technology*, **31**,
 613 doi:10.1175/JTECH-D-13-00230.1, 1410–1421.

- 614 Farrar, J. T., C. J. Zappa, R. A. Weller, and A. T. Jessup, 2007: Sea surface temperature signa-
615 tures of oceanic internal waves in low winds. *Journal of Geophysical Research: Oceans*, **112**,
616 doi:10.1029/2006JC003947.
- 617 Farrow, D. E., and J. C. Patterson, 1993: On the response of a reservoir sidearm to diurnal heating
618 and cooling. *J. Fluid Mech.*, **246**, 143–161.
- 619 Feddersen, F., 2012: Scaling surf zone turbulence. *Geophysical Research Letters*, **39**,
620 doi:10.1029/2012GL052970.
- 621 Feddersen, F., and R. T. Guza, 2003: Observations of nearshore circulation: Alongshore unifor-
622 mity. *Journal of Geophysical Research: Oceans*, **108**, doi:10.1029/2001JC001293, 6–1–6–10.
- 623 Feddersen, F., M. Olabarrieta, R. T. Guza, D. Winters, B. Raubenheimer, and S. Elgar, 2016:
624 Observations and modeling of a tidal inlet dye tracer plume. *Journal of Geophysical Research:*
625 *Oceans*, doi:10.1002/2016JC011922, n/a–n/a.
- 626 Fong, D. A., and M. T. Stacey, 2003: Horizontal dispersion of a near-bed coastal plume. *J. Fluid*
627 *Mech.*, **489**, 239–267.
- 628 Grant, S. B., J. H. Kim, B. H. Jones, S. A. Jenkins, J. Wasyl, and C. Cudaback, 2005: Surf
629 zone entrainment, along-shore transport, and human health implications of pollution from tidal
630 outlets. *J. Geophys. Res.*, **110**, doi:10.1029/2004JC002401.
- 631 Grimshaw, R., E. Pelinovsky, T. Talipova, and A. Kurkin, 2004: Simulation of the transforma-
632 tion of internal solitary waves on oceanic shelves. *Journal of Physical Oceanography*, **34**,
633 doi:10.1175/JPO2652.1, 2774–2791.
- 634 Hally-Rosendahl, K., F. Feddersen, D. B. Clark, and R. T. Guza, 2015: Surfzone to inner-shelf
635 exchange estimated from dye tracer balances. *Journal of Geophysical Research: Oceans*, **120**,
636 doi:10.1002/2015JC010844, 6289–6308.

- 637 Hally-Rosendahl, K., F. Feddersen, and R. T. Guza, 2014: Cross-shore tracer exchange
638 between the surfzone and inner-shelf. *Journal of Geophysical Research: Oceans*, **119**,
639 doi:10.1002/2013JC009722, 4367–4388.
- 640 Hendershott, M., 1981: *Long waves and ocean tides*. In "Evolution of Physical Oceanography"
641 (B.A. Warren and C. Wunsch, eds.), MIT Press, Cambridge, Mass., chapter 10. 292–341.
- 642 Henderson, S. M., 2016: Upslope internal-wave Stokes drift, and compensating downslope eu-
643 lerian mean currents, observed above a lakebed. *Journal of Physical Oceanography*, **46**,
644 doi:10.1175/JPO-D-15-0114.1, 1947–1961.
- 645 Holloway, P. E., E. Pelinovsky, and T. Talipova, 1999: A generalized Korteweg-de Vries model
646 of internal tide transformation in the coastal zone. *Journal of Geophysical Research: Oceans*,
647 **104**, doi:10.1029/1999JC900144, 18333–18350.
- 648 Horwitz, R., and S. J. Lentz, 2014: Inner-shelf response to cross-shelf wind stress: The importance
649 of the cross-shelf density gradient in an idealized numerical model and field observations. *Jour-
650 nal of Physical Oceanography*, **44**, doi:10.1175/JPO-D-13-075.1, 86–103.
- 651 Johnson, D., and C. Pattiaratchi, 2004: Transient rip currents and nearshore circulation on a swell-
652 dominated beach. *Journal of Geophysical Research: Oceans*, **109**, doi:10.1029/2003JC001798.
- 653 Jones, N. L., R. J. Lowe, G. Pawlak, D. A. Fong, and S. G. Monismith, 2008:
654 Plume dispersion on a fringing coral reef system. *Limnology and Oceanography*, **53**,
655 doi:10.4319/lo.2008.53.5_part_2.2273, 2273–2286.
- 656 Klymak, J. M., and J. N. Moum, 2003: Internal solitary waves of elevation advancing on a shoaling
657 shelf. *Geophysical Research Letters*, **30**, doi:10.1029/2003GL017706.
- 658 Kumar, N., and F. Feddersen, 2017a: The effect of Stokes drift and transient rip currents on the in-
659 ner shelf. part ii: With stratification. *Journal of Physical Oceanography*, **47**, doi:10.1175/JPO-

660 D-16-0077.1, 243–260.

661 — 2017b: A new offshore transport mechanism for shoreline-released tracer induced by transient
662 rip currents and stratification. *Geophys. Res. Lett.*, **44**, doi:10.1002/2017GL072611.

663 Kumar, N., F. Feddersen, S. Suanda, Y. Uchiyama, and J. McWilliams, 2016: Mid- to inner-shelf
664 coupled ROMS-SWAN model-data comparison of currents and temperature: Diurnal and semi-
665 diurnal variability. *J. Phys. Ocean.*, doi:10.1175/JPO-D-15-0103.1.

666 Lamb, K. G., 1997: Particle transport by nonbreaking, solitary internal waves. *Journal of Geo-
667 physical Research: Oceans*, **102**, doi:10.1029/97JC00441, 18641–18660.

668 Lentz, S. J., 2001: The influence of stratification on the wind-driven cross-shelf circulation
669 over the North Carolina shelf. *Journal of Physical Oceanography*, **31**, doi:10.1175/1520-
670 0485(2001)031<2749:TIOSOT>2.0.CO;2, 2749–2760.

671 Lentz, S. J., and M. R. Fewings, 2012: The wind- and wave-driven inner-shelf circulation. *Annual
672 Review of Marine Science*, **4**, doi:10.1146/annurev-marine-120709-142745, 317–343, pMID:
673 22457978.

674 Lerczak, J. A., M. C. Hendershott, and C. D. Winant, 2001: Observations and modeling of coastal
675 internal waves driven by a diurnal sea breeze. *Journal of Geophysical Research: Oceans*, **106**,
676 doi:10.1029/2001JC000811, 19715–19729.

677 Longuet-Higgins, M. S., 1970a: Longshore currents generated by obliquely incident sea waves: 1.
678 *Journal of Geophysical Research*, **75**, doi:10.1029/JC075i033p06778, 6778–6789.

679 — 1970b: Longshore currents generated by obliquely incident sea waves: 2. *Journal of Geophysi-
680 cal Research*, **75**, doi:10.1029/JC075i033p06790, 6790–6801.

681 Lucas, A. J., P. J. S. Franks, and C. L. Dupont, 2011: Horizontal internal-tide fluxes support
682 elevated phytoplankton productivity over the inner continental shelf. *Limnology and Oceanog-*

683 *raphy: Fluids and Environments*, **1**, doi:10.1215/21573698-1258185, 56–74.

684 Marmorino, G. O., G. B. Smith, and G. J. Lindemann, 2004: Infrared imagery of ocean internal
685 waves. *Geophysical Research Letters*, **31**, doi:10.1029/2004GL020152.

686 Melville, W. K., L. Lenain, D. R. Cayan, M. Kahru, J. P. Kleissl, P. F. Linden, and N. M. Statom,
687 2016: The modular aerial sensing system. *Journal of Atmospheric and Oceanic Technology*,
688 **33**, doi:10.1175/JTECH-D-15-0067.1, 1169–1184.

689 Molina, L., G. Pawlak, J. R. Wells, S. G. Monismith, and M. A. Merrifield, 2014: Diurnal cross-
690 shore thermal exchange on a tropical forereef. *Journal of Geophysical Research: Oceans*, **119**,
691 doi:10.1002/2013JC009621, 6101–6120.

692 Monismith, S. G., J. Imberger, and M. L. Morison, 1990: Convective motions in the sidearm of a
693 small reservoir. *Limnol. Oceanogr.*, **37**, 1676–1702.

694 Moniz, R. J., D. A. Fong, C. B. Woodson, S. K. Willis, M. T. Stacey, and S. G. Monismith, 2014:
695 Scale-dependent dispersion within the stratified interior on the shelf of northern monterey bay.
696 *Journal of Physical Oceanography*, **44**, doi:10.1175/JPO-D-12-0229.1, 1049–1064.

697 Morgan, S. G., A. L. Shanks, J. H. MacMahan, A. J. Reniers, and F. Feddersen, 2018: Plank-
698 tonic subsidies to surf-zone and intertidal communities. *Annual Review of Marine Science*, **10**,
699 doi:10.1146/annurev-marine-010816-060514, null, PMID: 28846492.

700 Nam, S., and U. Send, 2011: Direct evidence of deep water intrusions onto the conti-
701 nental shelf via surging internal tides. *Journal of Geophysical Research: Oceans*, **116**,
702 doi:10.1029/2010JC006692.

703 Omand, M. M., J. J. Leichter, P. J. S. Franks, R. T. Guza, A. J. Lucas, and F. Feddersen, 2011:
704 Physical and biological processes underlying the sudden surface appearance of a red tide in the
705 nearshore. *Limnology and Oceanography*, **56**, doi:10.4319/lo.2011.56.3.0787, 787–801.

- 706 Pineda, J., 1999: Circulation and larval distribution in internal tidal bore warm fronts. *Limnology*
707 *and Oceanography*, **44**, doi:10.4319/lo.1999.44.6.1400, 1400–1414.
- 708 Pineda, J., J. A. Hare, and S. Sponaugle, 2007: Larval transport and dispersal in the coastal ocean
709 and consequences for population connectivity. *Oceanography*, **20**.
- 710 Rainville, L., and R. Pinkel, 2001: Wirewalker: An autonomous wave-powered verti-
711 cal profiler. *Journal of Atmospheric and Oceanic Technology*, **18**, doi:10.1175/1520-
712 0426(2001)018<1048:WAAWPV>2.0.CO;2, 1048–1051.
- 713 Shroyer, E. L., J. N. Moum, and J. D. Nash, 2010: Vertical heat flux and lateral mass transport in
714 nonlinear internal waves. *Geophysical Research Letters*, **37**, doi:10.1029/2010GL042715.
- 715 Sinnett, G., F. Feddersen, A. J. Lucas, G. Pawlak, and E. Terrill, 2018: Observations of nonlinear
716 internal wave run-up to the surfzone. *Journal of Physical Oceanography*, **48**, doi:10.1175/JPO-
717 D-17-0210.1, 531–554.
- 718 Smith, R. L., 1981: *A Comparison of the Structure and Variability of the Flow Field in three*
719 *Coastal Upwelling Regions: Oregon, Northwest Africa, and Peru*, American Geophysical
720 Union (AGU). doi:10.1029/CO001p0107, 107–118.
- 721 Stacey, M. T., E. A. Cowen, T. M. Powell, E. Dobbins, S. G. Monismith, and J. R. Koseff, 2000:
722 Plume dispersion in a stratified, near-coastal flow: measurements and modeling. *Continental*
723 *Shelf Research*, **20**, doi:https://doi.org/10.1016/S0278-4343(99)00061-8, 637 – 663.
- 724 Suanda, S. H., and F. Feddersen, 2015: A self-similar scaling for cross-shelf exchange driven by
725 transient rip currents. *Geophysical Research Letters*, **42**, doi:10.1002/2015GL063944, 5427–
726 5434, 2015GL063944.
- 727 Suanda, S. H., F. Feddersen, and N. Kumar, 2017: The effect of barotropic and baroclinic
728 tides on coastal stratification and mixing. *Journal of Geophysical Research: Oceans*, **122**,

729 doi:10.1002/2017JC013379, 10156–10173.

730 Sundermeyer, M. A., and J. R. Ledwell, 2001: Lateral dispersion over the continental shelf:
731 Analysis of dye release experiments. *Journal of Geophysical Research: Oceans*, **106**,
732 doi:10.1029/2000JC900138, 9603–9621.

733 Sutherland, B. R., K. J. Barrett, and G. N. Ivey, 2013: Shoaling internal solitary waves. *J. Geo-*
734 *phys. Res.*, **118**, doi:10.1002/jgrc.20291, 4111–4124.

735 Thorpe, S. A., 1999: The generation of alongslope currents by breaking internal waves. *Journal of*
736 *Physical Oceanography*, **29**, doi:10.1175/1520-0485(1999)029<0029:TGOACB>2.0.CO;2,
737 29–38.

738 Ulloa, H. N., K. A. Davis, S. G. Monismith, and G. Pawlak, 2018: Temporal variability in
739 thermally driven cross-shore exchange: The role of semidiurnal tides. *Journal of Physical*
740 *Oceanography*, **48**, doi:10.1175/JPO-D-17-0257.1, 1513–1531.

741 Walsh, E. J., R. Pinkel, D. E. Hagan, R. A. Weller, C. W. Fairall, D. P. Rogers, S. P. Burns, and
742 M. Baumgartner, 1998: Coupling of internal waves on the main thermocline to the diurnal
743 surface layer and sea surface temperature during the tropical ocean-global atmosphere cou-
744 pled ocean-atmosphere response experiment. *Journal of Geophysical Research: Oceans*, **103**,
745 doi:10.1029/98JC00894, 12613–12628.

746 Walter, R. K., E. C. Reid, K. A. Davis, K. J. Armenta, K. Merhoff, and N. J. Nidzieko, 2017:
747 Local diurnal wind-driven variability and upwelling in a small coastal embayment. *Journal of*
748 *Geophysical Research: Oceans*, **122**, doi:10.1002/2016JC012466, 955–972.

749 Walter, R. K., C. B. Woodson, R. S. Arthur, O. B. Fringer, and S. G. Monismith, 2012: Nearshore
750 internal bores and turbulent mixing in southern monterey bay. *Journal of Geophysical Re-*
751 *search: Oceans*, **117**, doi:10.1029/2012JC008115, n/a–n/a, c07017.

752 Washburn, L., and E. McPhee-Shaw, 2013: Coastal transport processes affecting inner-shelf
753 ecosystems in the california current system. *Oceanography*, **26**, 34–43.

754 Winant, C. D., 1974: Internal surges in coastal waters. *Journal of Geophysical Research*, **79**,
755 doi:10.1029/JC079i030p04523, 4523–4526.

756 Wunsch, C., 1971: Note on some reynolds stress effects of internal waves on slopes. *Deep Sea*
757 *Research and Oceanographic Abstracts*, **18**, doi:https://doi.org/10.1016/0011-7471(71)90124-
758 0, 583 – 591.

759 Zhang, S., M. H. Alford, and J. B. Mickett, 2015: Characteristics, generation and mass transport of
760 nonlinear internal waves on the washington continental shelf. *Journal of Geophysical Research:*
761 *Oceans*, **120**, doi:10.1002/2014JC010393, 741–758.

762 Zikanov, O., and D. N. Slinn, 2001: Along-slope current generation by obliquely incident internal
763 waves. *Journal of Fluid Mechanics*, **445**, doi:10.1017/S0022112001005560, 235–261.

764
765
766 Generated with ametsocjmk.cls.
767 Written by J. M. Klymak
768 mailto:jklymak@ucsd.edu
769 http://opgl.ucsd.edu/jklymak/WorkTools.html

Figure Captions

FIG. 1. (a) Map of San Diego Bight study region, with inset to illustrate location of experiment with respect to the California (US)–Baja California (MX) coast. The dye release location R2 (magenta circle), the local (x,y) coordinate axes with lengths of (2, 4) km in white, and white dashed line shows perimeter of panel (b). Indicated are the locations of offshore fixed instrumentation: two wire-walkers (W1 & W2), thermistor mooring (Tr), Coastal Data Information Program (CDIP) wave buoy, and TRNERR meteorological (MET) station. Also shown in (a) are SZ instruments M4 & M5 (orange), north of panel (b). Bathymetry is derived from the 2012 NOAA tsunami DEM and $h = [6, 12, 24, 36, \dots]$ m are contoured in black. (b) Map of surface dye field at 10:20 PDT on Oct. 08, 2015 contoured in parts-per-billion, along with the locations of IS current meter (ADCP), and SZ instrumentation (M1-M3 & S1-S3). Also shown in (b) are the raw trajectories of the towed array (TA) and autonomous-underwater vehicle (AUV) transects.

FIG. 2. Example of spatial filter applied to the IS surface dye field at 1020 h ($t_r = 5.02$ h): (a) surface dye concentration $D(x, y)$ from calibrated MASS hyperspectral imagery; (b) large-scale dye field \bar{D} with cut-off of 150 m; (c) small-scale dye field D' versus x and y . The same color scale (0-12 ppb) is used in (a)-(b), and in (c) the scale is ± 2 ppb. In (a)-(c) gray is land, and black bathymetry contours are $h = [2, 6, 12]$ m, magenta is the release location, and the location of ADCP (\diamond) and IS moorings Tr (+) and W1 (yellow) are also indicated.

FIG. 3. Five-day time-series of CSIDE experiment conditions: (a) TRNERR MET station wind vectors (see Fig. 1) where the line color represents the hour of day; (b) significant wave height (H_s) from CDIP buoy; (c) sea-surface elevation (η) from ADCP pressure record; (d) band-passed mid-depth temperature \bar{T}_{mid} evolution at Tr (black), W1 (blue), and W2 (red). The time-period spanning the release R2 is denoted with a magenta bar, and the IS plume deformation period with the gray bar.

FIG. 4. Large-scale (a) temperature \bar{T} at mooring Tr (white cross in Figs. 1, 2-6) with contours at 0.25 °C intervals, and (b) cross-shore velocity \bar{u} at ADCP (white diamond in Figs. 1 and 6) adjacent to Tr, with contours at 2.5 cm s⁻¹ intervals. In (a)-(b) green dots indicate approximate instrument sample depths, and the dashed black lines are average $\bar{T} = 20.5$ °C isotherm slopes of 1.5 m h⁻¹ and -0.7 m h⁻¹ during the release (magenta bar, top) and deformation (gray bar, top) periods, respectively. (c) Raw temperature versus time at the release location (magenta), with low pass-filtered upper Tr thermistor ($z = -2.6$ m, blue); and temperature derived from the large-scale filtered and alongshore average SZ instruments (black curve) \pm the 30 min running rms deviation

from the mean (gray shading). In (c) the AUV (red) and TA (cyan) transect times are indicated by horizontal bars.

FIG. 5. Surface dye concentration D versus horizontal coordinates (x, y) during (a)-(c) deformation period; and (d) ≈ 12 h after dye release began. Time is indicated above each panel in hhmm relative to Pacific Daylight Time (PDT \rightarrow h), corresponding to $t_r = [5.02, 5.50, 6.60, 11.65]$ h, respectively. Note the difference in scales in panel (d). Release location (magenta dot), IS temperature mooring Tr (+), current meter ADCP (\diamond), and wire-walker W1 (yellow) are indicated. Land is dark gray, oceanic regions without data are light gray, and bathymetry contours (black) are drawn at 2 m intervals below mean sea-level.

FIG. 6. (a)-(d) Large-scale IS surface dye \bar{D} evolution during deformation period versus x and y . In each panel time is relative to PDT, corresponding to $t_r = [5.02, 5.59, 6.09, 6.75]$ h, respectively. The 1 ppb contour (thick black) at each time along with all prior contours (thin black) are shown to indicate deformation. The magenta dot $(x, y) = (0, 0)$ is the release location. Also drawn are the average locations of the AUV transect (dashed red line), alongshore TA transect (dashed cyan line), and the gray dashed line is the MASS transect. Dark gray indicates land and the bathymetry is contoured at 2 m intervals below mean sea-level.

FIG. 7. AUV transect large-scale (left, (a)-(b)) dye concentration \bar{D} with contours at 1 ppb intervals, and (right, (c)-(d)) temperature \bar{T} with contours at 0.25°C intervals versus local cross-shore coordinate \tilde{x} and vertical coordinate \tilde{z} at (top, (a) & (c)) $t = 1049$ h ($t_r = 5.50$ h) and (bottom, (b) & (d)) $t = 1151$ h ($t_r = 6.54$ h). The AUV transect line is shown as red dashed line in Fig. 6 and each transect took approximately 20 min. In (c) and (d) the dashed lines are the average $T = 20.5^\circ\text{C}$ isotherm slopes with values (c) 1.44 m km^{-1} and (d) -2.3 m km^{-1} . The approximate cross-shore location of TA (cyan, Fig. 8) is indicated in (b) & (d).

FIG. 8. TA transect Large-scale (a) temperature \bar{T} with contours at 0.25°C and (b) dye \bar{D} with contours at 2 ppb versus depth \tilde{z} and alongshore coordinate y . TA transect line is shown in Figs. 1a & 6. The transect began at $t = 1107$ h ($t_r = 5.80$ h) and the elapsed time is marked on top. Instrument locations are indicated by green circles on left axis, and the black dashed line in (a) is the slope of the $\bar{T} = 20.5^\circ\text{C}$ contour, -1.20 m km^{-1} or -2.82 m h^{-1} .

FIG. 9. Dye versus temperature and time on morning of R2 from the SZ (black), at TA (blue), and AUV (red). Thick markers represent arithmetic mean temperature (*i.e.*, $E[T]$, where $E[\]$ is the averaging operator) and logarithmic mean dye (*i.e.*, $\exp(E[\log(D)])$) of observations where $D \geq 1$ ppb, evaluated at approximately 44 min intervals ($t_r = [4.39, 5.10, 5.84, 6.59]$ h), and the

dashes represent ± 1 standard-deviation over the same interval. TA and AUV transect data from 0942 h ($t_r = 4.39$ h, red and blue circles) prior the deformation period and before aerial sampling began are included here for comparison with SZ observations.

FIG. 10. Surface (a) dye concentration and (b) relative temperature versus local cross-shore coordinate \tilde{x} at multiple times (see colorbar in (a)) during the deformation period. In (a) the surface dye concentration (measured in parts-per-billion (ppb)) of each curve is offset by -3 ppb (earliest observation is upper-most curve), in (b) the surface temperature is relative to 1 km offshore and each curve is offset by 0.1 °C, in (a)-(b) the red dashed curve is the offshore location of $\bar{D} = 1$ ppb (see black contour in Fig. 6) and the blue dashed curve is the location of \bar{D}_{\max} . The dashed black lines have $\partial\bar{T}/\partial\tilde{x} = -0.38$ & 0.2 °C km $^{-1}$ between $\tilde{x} = -800$ m and -100 m and correspond to $t = 1020$ h & 1217 h, respectively.

FIG. 11. Cross-shore maximum of the mean surface dye concentration \bar{D} versus y during the deformation period, where the color of each curve indicates time of observation shown in the legend, red arrows indicate (left-to-right) -6.5 , -1.5 , and 3 cm s $^{-1}$, illustrating an alongshore plume strain rate of approximately 5 cm s $^{-1}$ km $^{-1}$.

FIG. 12. Small-scale temperature T' at thermistor string Tr (white cross in Figs. 1, 2– 6) as a function of depth and time. The horizontal magenta, and gray bars span the release and deformation periods, respectively, and the dashed black line is the average slope of the $\bar{T} = 20.5$ °C isotherm (see Fig. 4). The dotted black line is the 3h large-scale filtered vertical location of maximum temperature stratification.

FIG. 13. Snap-shot of (a) small-scale dye gradient $\partial D'/\partial x$ and (b) small-scale temperature gradient $\partial T'/\partial x$ versus x and y at $t = 1155$ h ($t_r = 6.60$ h). The cross-shore MASS transect is indicated with a gray dashed line and $\bar{D} = 1$ ppb contour shown in black (*e.g.*, see Fig. 6). Location of moorings Tr (white, +) and W1 (yellow, o) and dye release (magenta dot) are also indicated.

FIG. 14. Small-scale dye $\partial D'/\partial\tilde{x}$ (a) and temperature $\partial T'/\partial\tilde{x}$ (b) on cross-shore MASS transect (dashed line in Fig. 13) versus local, shoreline referenced cross-shore coordinate \tilde{x} and time t during deformation period. The dashed black line indicates an onshore progression of 9 cm s $^{-1}$.

FIG. 15. Time root-mean-square of the cross-shore, small-scale temperature gradient $\text{rms}(\partial T'/\partial x)$ during the deformation period $1020 \leq t \leq 1217$ h. The rms estimate was derived from 27 MASS passes of surface $\partial T'/\partial x$, and regions with fewer than 25 samples were removed prior

to applying the large-scale spatial filter described in Section 2d. Light gray are regions without data and the wake of the Imperial Beach pier at $y \approx -1$ km and land has been masked in dark gray.

Figures

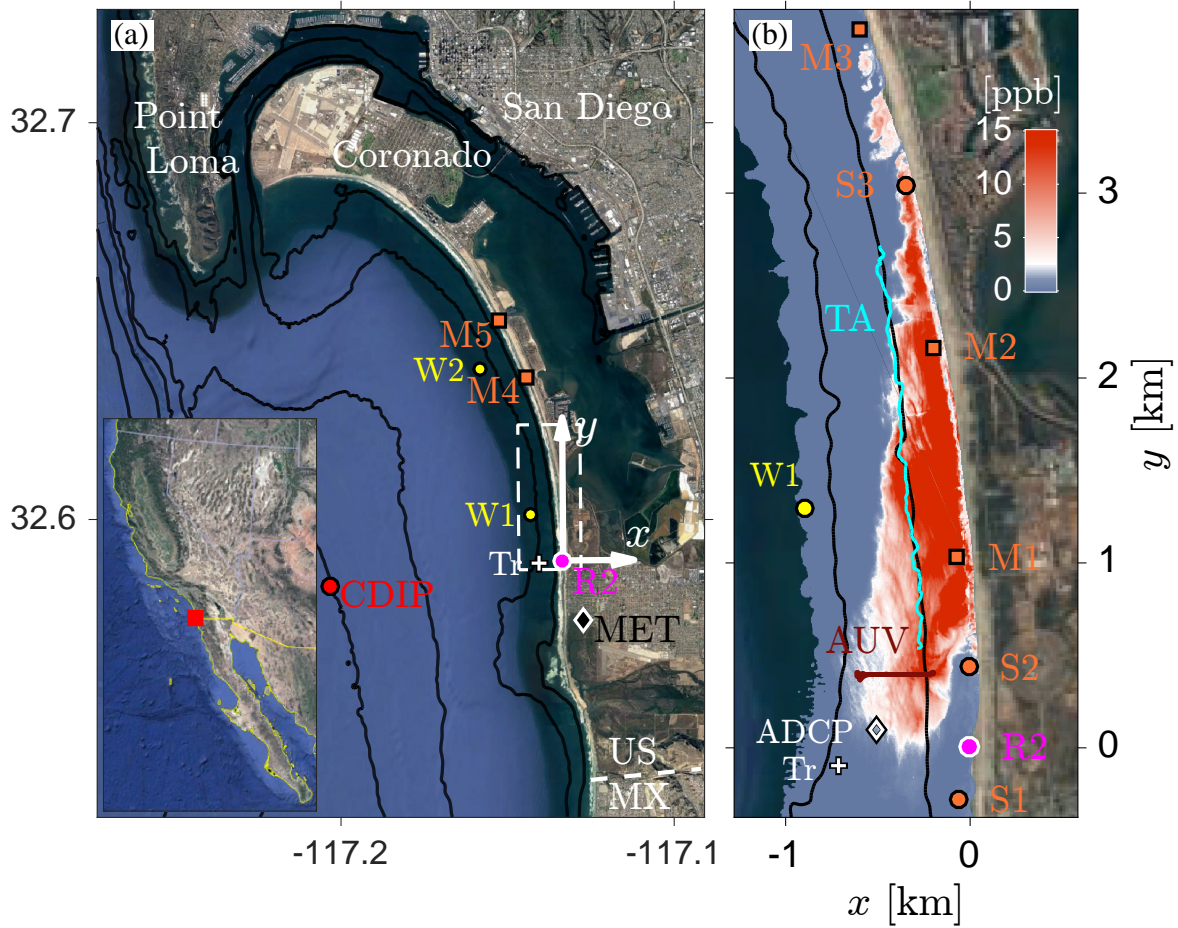


FIG. 1. (a) Map of San Diego Bight study region, with inset to illustrate location of experiment with respect to the California (US)–Baja California (MX) coast. The dye release location R2 (magenta circle), the local (x,y) coordinate axes with lengths of (2, 4) km in white, and white dashed line shows perimeter of panel (b). Indicated are the locations of offshore fixed instrumentation: two wire-walkers (W1 & W2), thermistor mooring (Tr), Coastal Data Information Program (CDIP) wave buoy, and TRNERR meteorological (MET) station. Also shown in (a) are SZ instruments M4 & M5 (orange), north of panel (b). Bathymetry is derived from the 2012 NOAA tsunami DEM and $h = [6, 12, 24, 36, \dots]$ m are contoured in black. (b) Map of surface dye field at 10:20 PDT on Oct. 08, 2015 contoured in parts-per-billion, along with the locations of IS current meter (ADCP), and SZ instrumentation (M1-M3 & S1-S3). Also shown in (b) are the raw trajectories of the towed array (TA) and autonomous-underwater vehicle (AUV) transects.

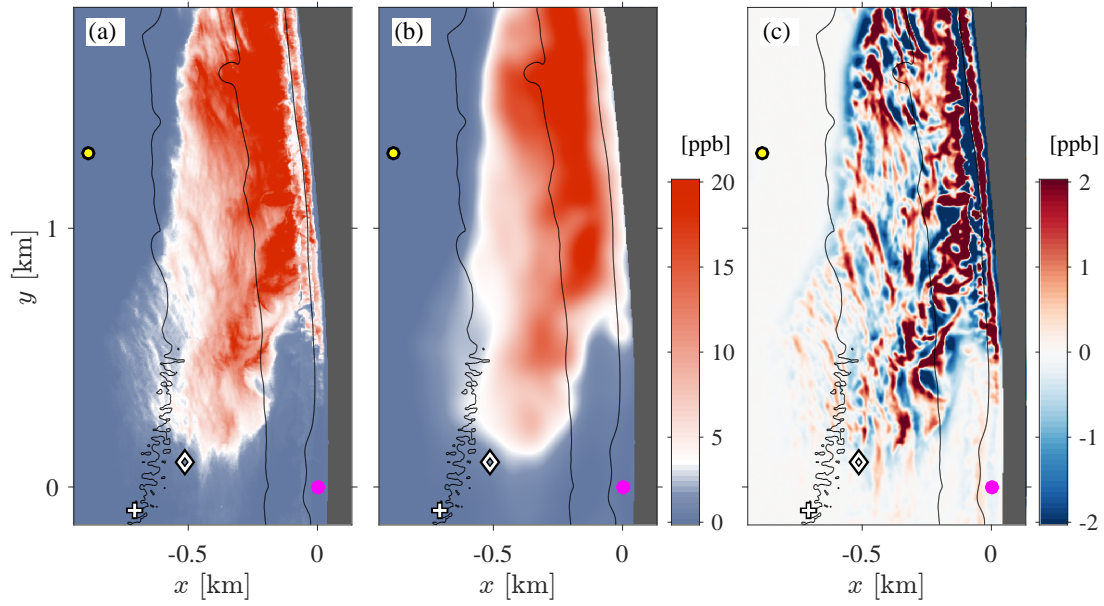


FIG. 2. Example of spatial filter applied to the IS surface dye field at 1020 h ($t_r = 5.02$ h): (a) surface dye concentration $D(x, y)$ from calibrated MASS hyperspectral imagery; (b) large-scale dye field \bar{D} with cut-off of 150 m; (c) small-scale dye field D' versus x and y . The same color scale (0-12 ppb) is used in (a)-(b), and in (c) the scale is ± 2 ppb. In (a)-(c) gray is land, and black bathymetry contours are $h = [2, 6, 12]$ m, magenta is the release location, and the location of ADCP (\diamond) and IS moorings Tr (+) and W1 (yellow) are also indicated.

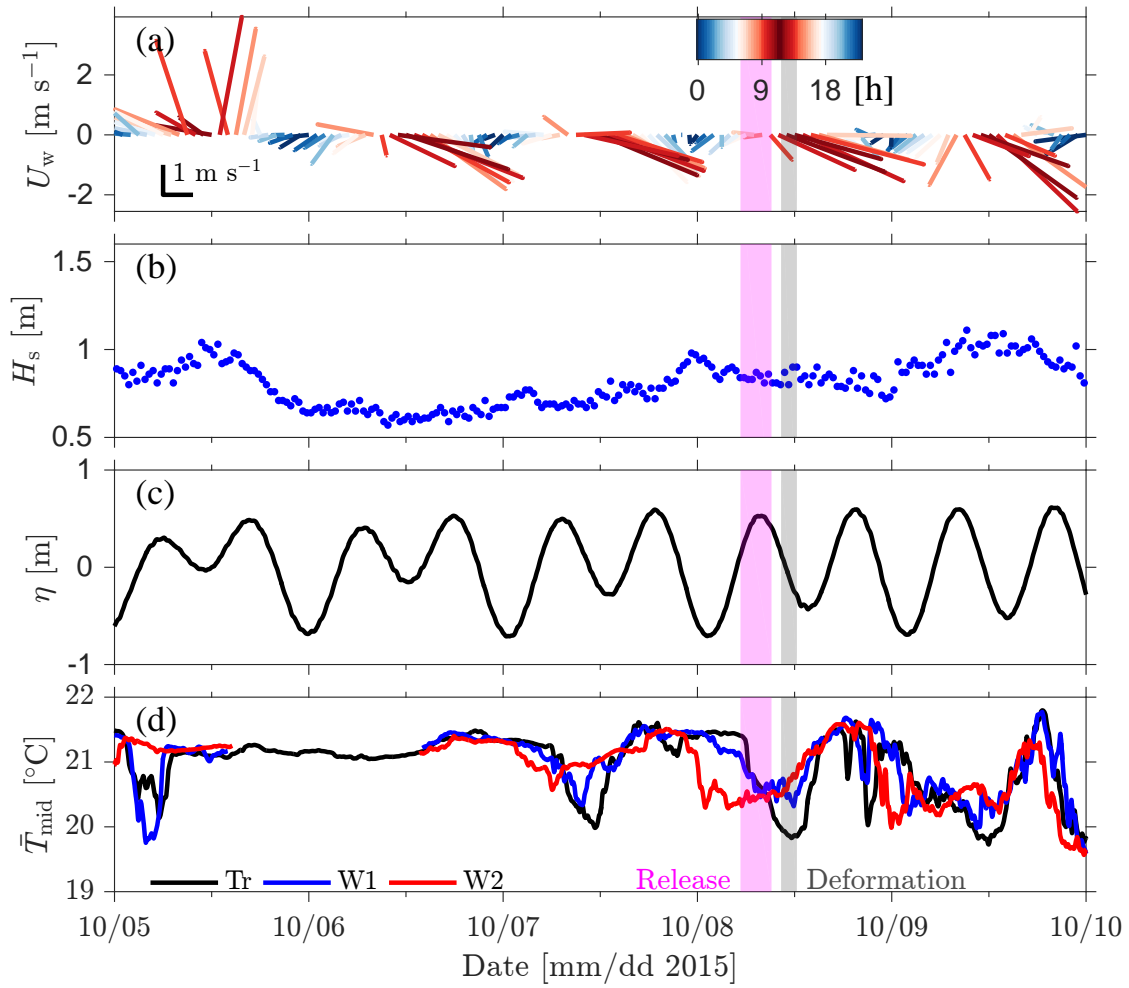


FIG. 3. Five-day time-series of CSIDE experiment conditions: (a) TRNERR MET station wind vectors (see Fig. 1) where the line color represents the hour of day; (b) significant wave height (H_s) from CDIP buoy; (c) sea-surface elevation (η) from ADCP pressure record; (d) band-passed mid-depth temperature \bar{T}_{mid} evolution at Tr (black), W1 (blue), and W2 (red). The time-period spanning the release R2 is denoted with a magenta bar, and the IS plume deformation period with the gray bar.

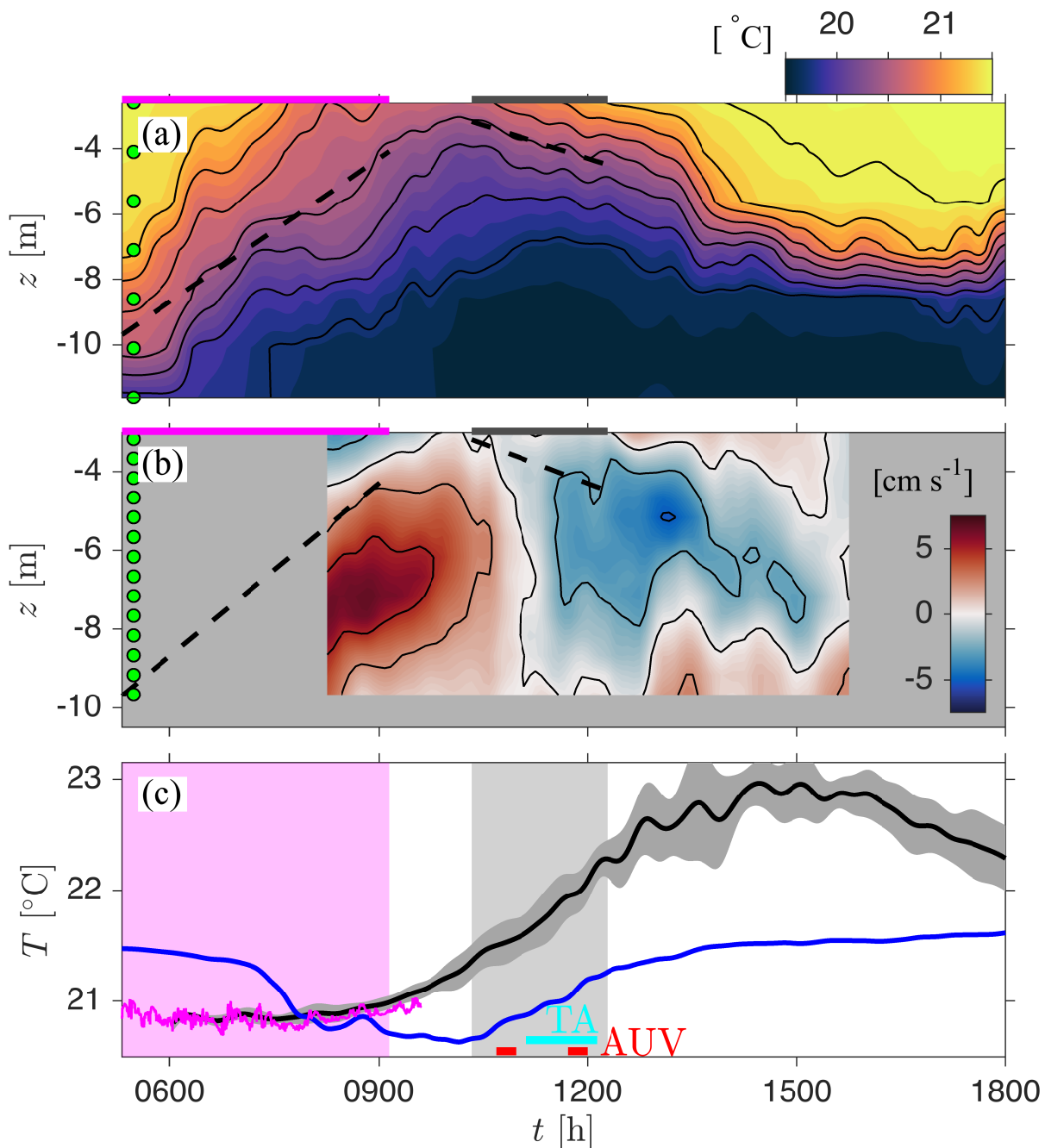


FIG. 4. Large-scale (a) temperature \bar{T} at mooring Tr (white cross in Figs. 1, 2-6) with contours at 0.25 °C intervals, and (b) cross-shore velocity \bar{u} at ADCP (white diamond in Figs. 1 and 6) adjacent to Tr, with contours at 2.5 cm s⁻¹ intervals. In (a)-(b) green dots indicate approximate instrument sample depths, and the dashed black lines are average $\bar{T} = 20.5$ °C isotherm slopes of 1.5 m h⁻¹ and -0.7 m h⁻¹ during the release (magenta bar, top) and deformation (gray bar, top) periods, respectively. (c) Raw temperature versus time at the release location (magenta), with low pass-filtered upper Tr thermistor ($z = -2.6$ m, blue); and temperature derived from the large-scale filtered and alongshore average SZ instruments (black curve) \pm the 30 min running rms deviation from the mean (gray shading). In (c) the AUV (red) and TA (cyan) transect times are indicated by horizontal bars.

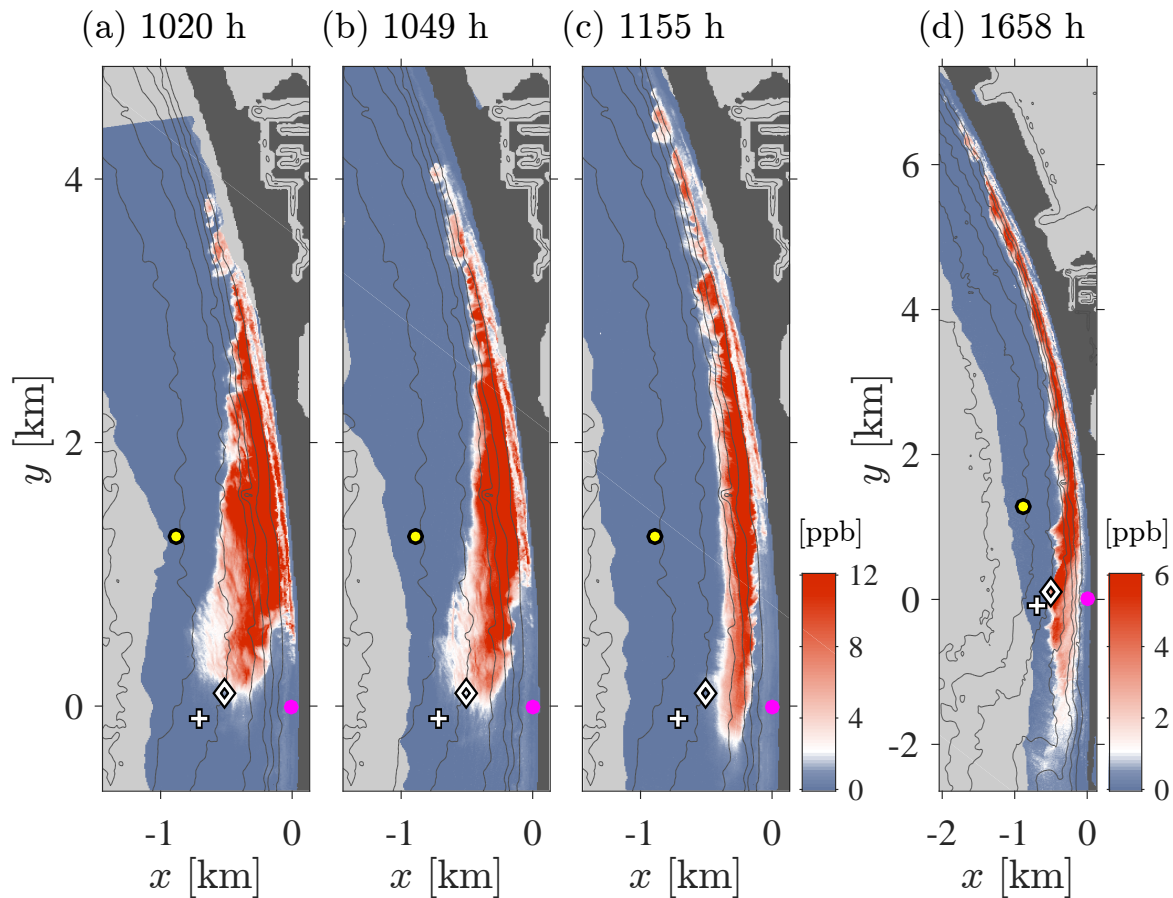


FIG. 5. Surface dye concentration D versus horizontal coordinates (x, y) during (a)-(c) deformation period; and (d) ≈ 12 h after dye release began. Time is indicated above each panel in hhmm relative to Pacific Daylight Time (PDT \rightarrow h), corresponding to $t_r = [5.02, 5.50, 6.60, 11.65]$ h, respectively. Note the difference in scales in panel (d). Release location (magenta dot), IS temperature mooring Tr (+), current meter ADCP (\diamond), and wire-walker W1 (yellow) are indicated. Land is dark gray, oceanic regions without data are light gray, and bathymetry contours (black) are drawn at 2 m intervals below mean sea-level.

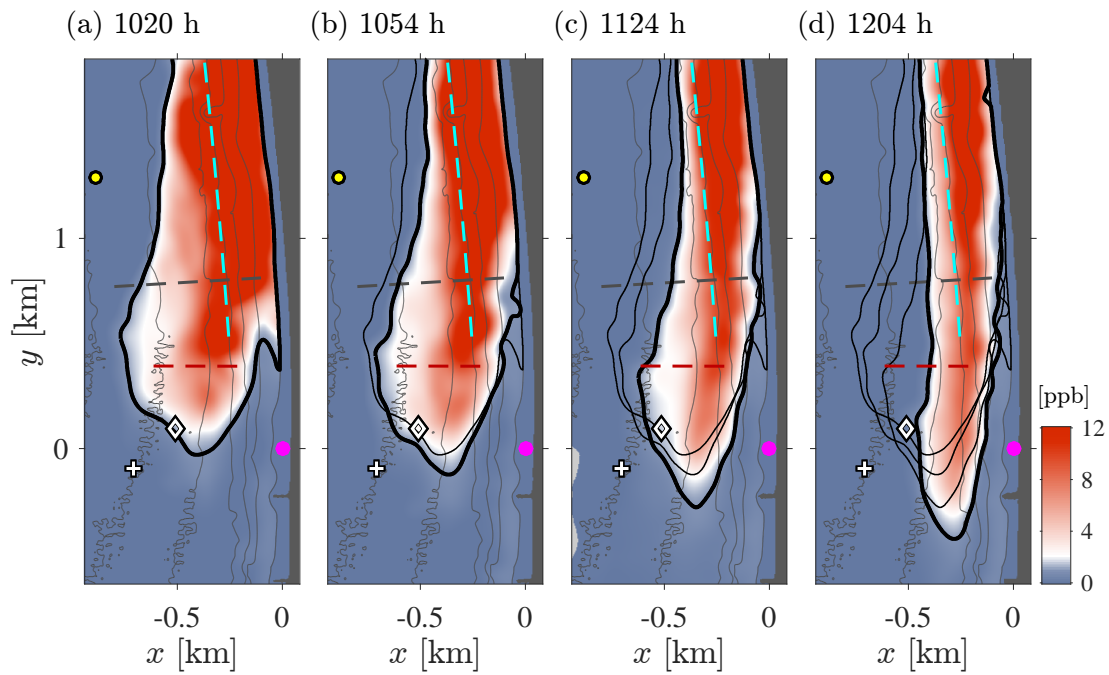


FIG. 6. (a)-(d) Large-scale IS surface dye \bar{D} evolution during deformation period versus x and y . In each panel time is relative to PDT, corresponding to $t_r = [5.02, 5.59, 6.09, 6.75]$ h, respectively. The 1 ppb contour (thick black) at each time along with all prior contours (thin black) are shown to indicate deformation. The magenta dot $(x, y) = (0, 0)$ is the release location. Also drawn are the average locations of the AUV transect (dashed red line), alongshore TA transect (dashed cyan line), and the gray dashed line is the MASS transect. Dark gray indicates land and the bathymetry is contoured at 2 m intervals below mean sea-level.

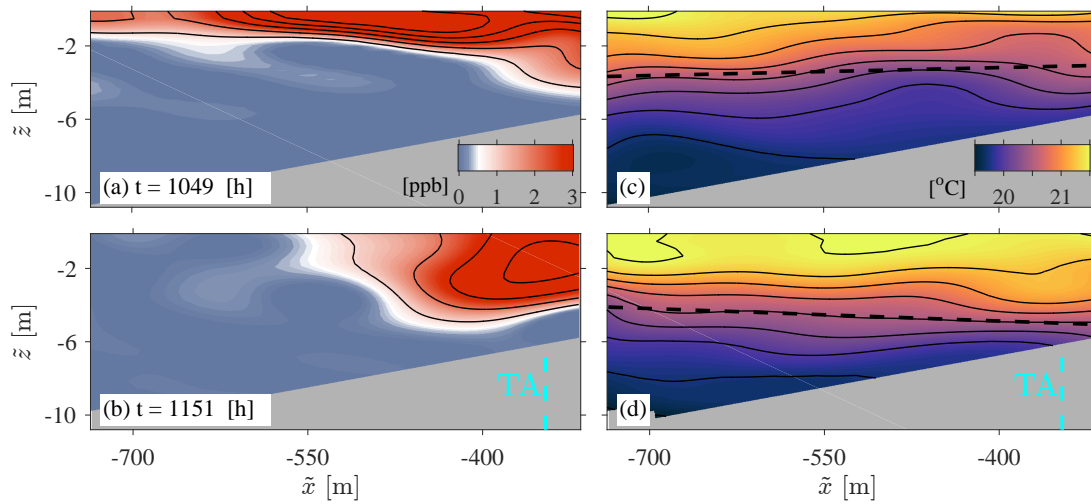


FIG. 7. AUV transect large-scale (left, (a)-(b)) dye concentration \bar{D} with contours at 1 ppb intervals, and (right, (c)-(d)) temperature \bar{T} with contours at 0.25 °C intervals versus local cross-shore coordinate \tilde{x} and vertical coordinate \tilde{z} at (top, (a) & (c)) $t = 1049$ h ($t_r = 5.50$ h) and (bottom, (b) & (d)) $t = 1151$ h ($t_r = 6.54$ h). The AUV transect line is shown as red dashed line in Fig. 6 and each transect took approximately 20 min. In (c) and (d) the dashed lines are the average $T = 20.5$ °C isotherm slopes with values (c) 1.44 m km $^{-1}$ and (d) -2.3 m km $^{-1}$. The approximate cross-shore location of TA (cyan, Fig. 8) is indicated in (b) & (d).

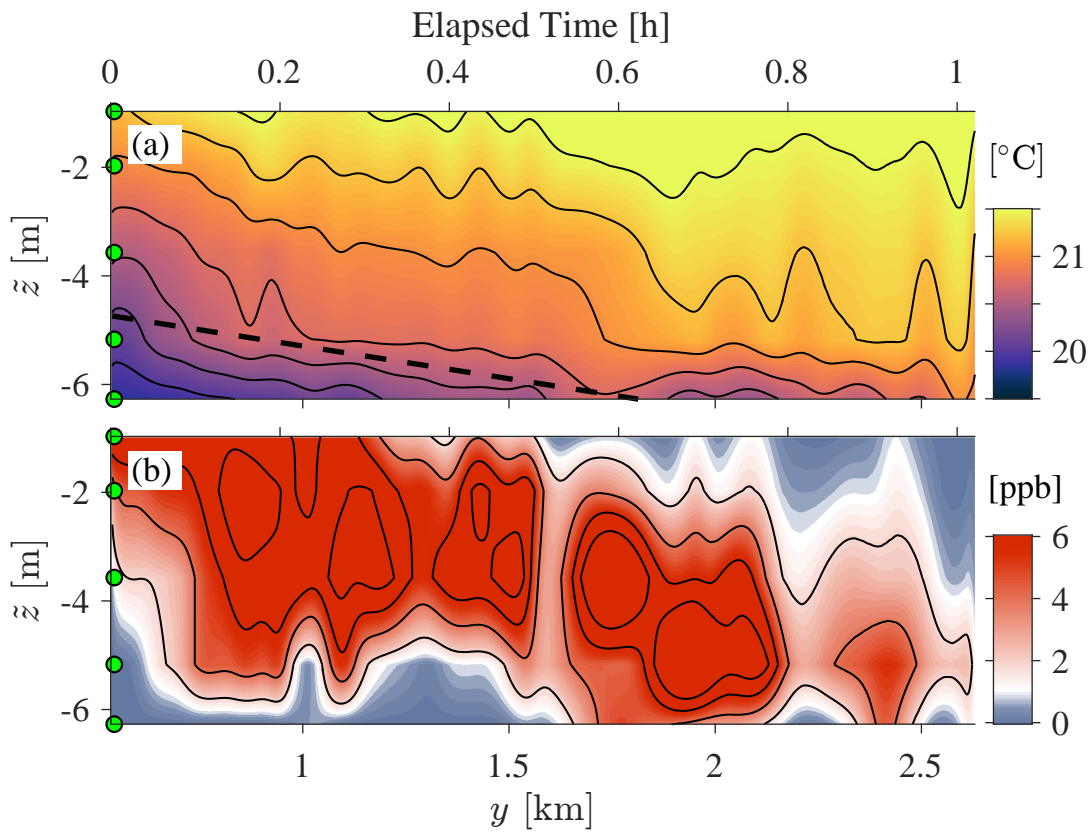


FIG. 8. TA transect Large-scale (a) temperature \bar{T} with contours at $0.25\text{ }^{\circ}\text{C}$ and (b) dye \bar{D} with contours at 2 ppb versus depth \tilde{z} and alongshore coordinate y . TA transect line is shown in Figs. 1a & 6. The transect began at $t = 1107\text{ h}$ ($t_r = 5.80\text{ h}$) and the elapsed time is marked on top. Instrument locations are indicated by green circles on left axis, and the black dashed line in (a) is the slope of the $\bar{T} = 20.5\text{ }^{\circ}\text{C}$ contour, -1.20 m km^{-1} or -2.82 m h^{-1} .

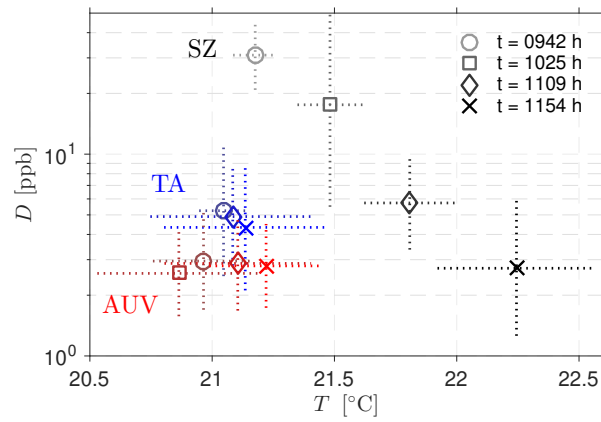


FIG. 9. Dye versus temperature and time on morning of R2 from the SZ (black), at TA (blue), and AUV (red). Thick markers represent arithmetic mean temperature (*i.e.*, $E[T]$, where $E[\cdot]$ is the averaging operator) and logarithmic mean dye (*i.e.*, $\exp(E[\log(D)])$) of observations where $D \geq 1$ ppb, evaluated at approximately 44 min intervals ($t_r = [4.39, 5.10, 5.84, 6.59]$ h), and the dashes represent ± 1 standard-deviation over the same interval. TA and AUV transect data from 0942 h ($t_r = 4.39$ h, red and blue circles) prior the deformation period and before aerial sampling began are included here for comparison with SZ observations.

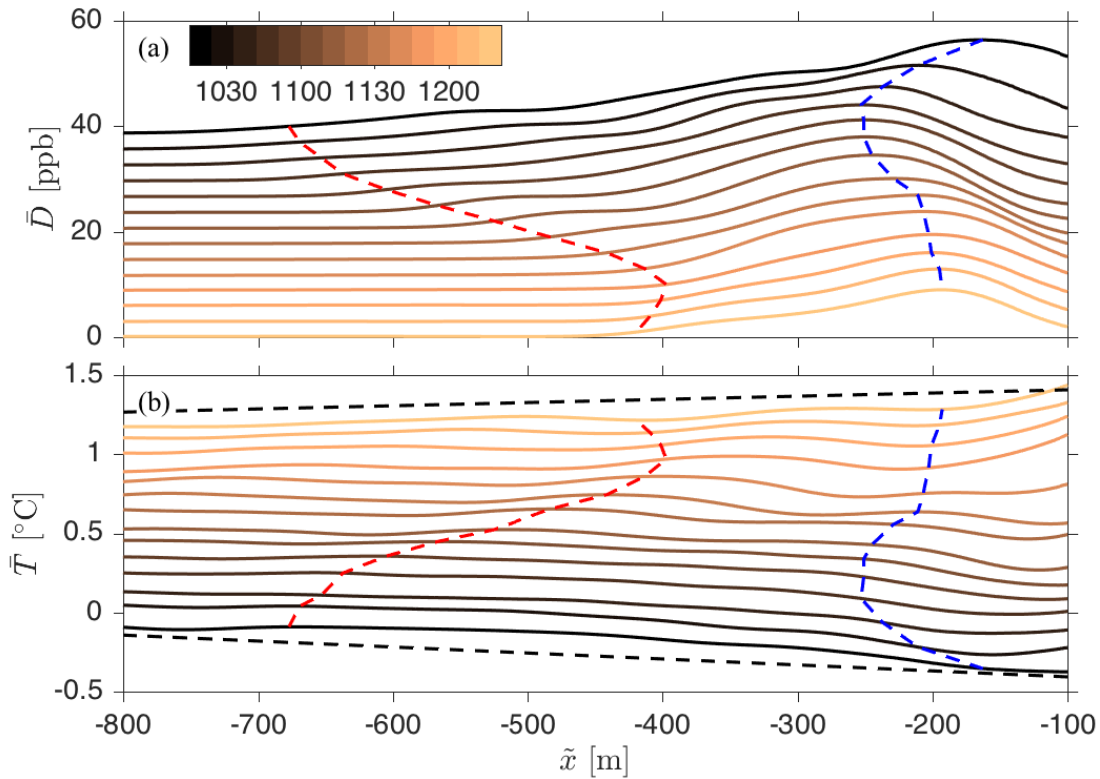


FIG. 10. Surface (a) dye concentration and (b) relative temperature versus local cross-shore coordinate \tilde{x} at multiple times (see colorbar in (a)) during the deformation period. In (a) the surface dye concentration (measured in parts-per-billion (ppb)) of each curve is offset by -3 ppb (earliest observation is upper-most curve), in (b) the surface temperature is relative to 1 km offshore and each curve is offset by 0.1 °C, in (a)-(b) the red dashed curve is the offshore location of $\bar{D} = 1$ ppb (see black contour in Fig. 6) and the blue dashed curve is the location of \bar{D}_{\max} . The dashed black lines have $\partial\bar{T}/\partial\tilde{x} = -0.38$ & 0.2 °C km⁻¹ between $\tilde{x} = -800$ m and -100 m and correspond to $t = 1020$ h & 1217 h, respectively.

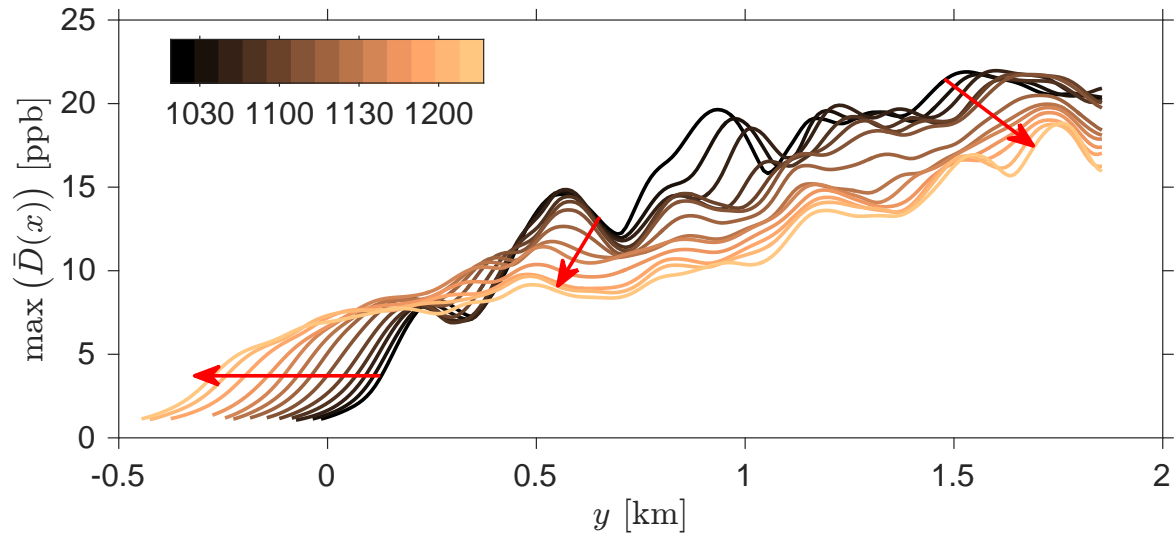


FIG. 11. Cross-shore maximum of the mean surface dye concentration \bar{D} versus y during the deformation period, where the color of each curve indicates time of observation shown in the legend, red arrows indicate (left-to-right) -6.5 , -1.5 , and 3 cm s^{-1} , illustrating an alongshore plume strain rate of approximately $5 \text{ cm s}^{-1} \text{ km}^{-1}$.

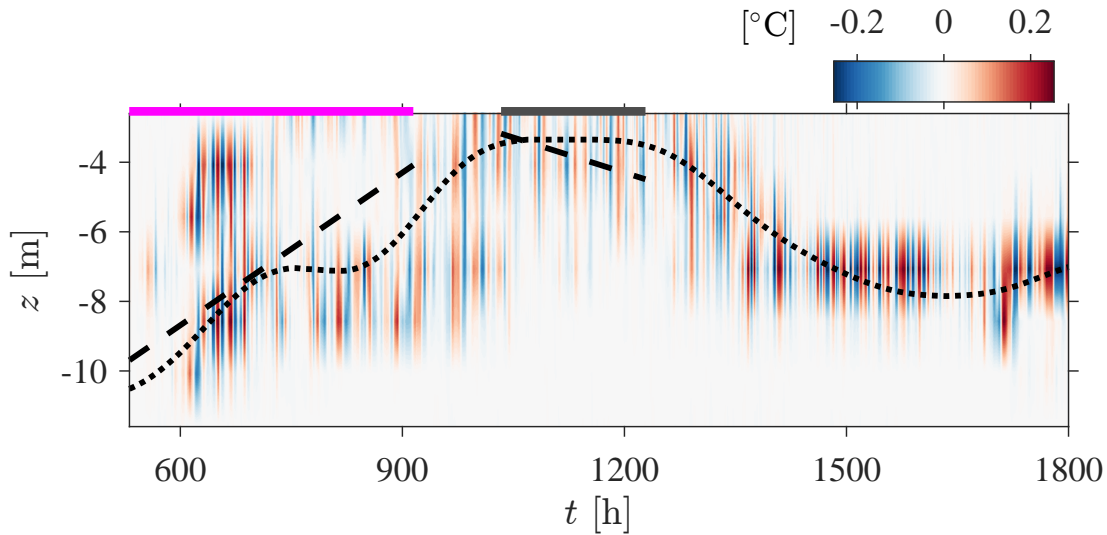


FIG. 12. Small-scale temperature T' at thermistor string Tr (white cross in Figs. 1, 2–6) as a function of depth and time. The horizontal magenta, and gray bars span the release and deformation periods, respectively, and the dashed black line is the average slope of the $\bar{T} = 20.5 \text{ }^\circ\text{C}$ isotherm (see Fig. 4). The dotted black line is the 3h large-scale filtered vertical location of maximum temperature stratification.

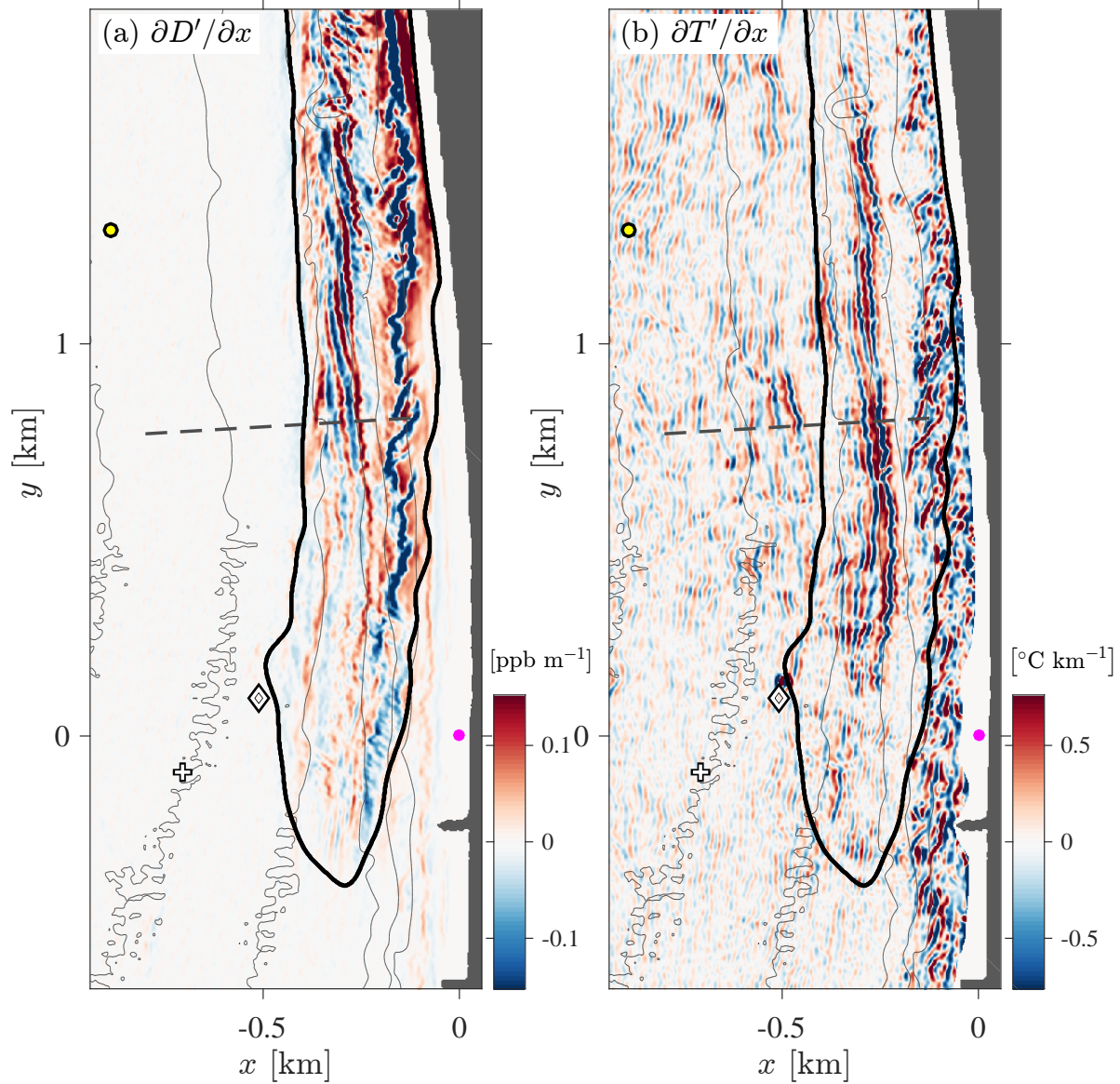


FIG. 13. Snap-shot of (a) small-scale dye gradient $\partial D'/\partial x$ and (b) small-scale temperature gradient $\partial T'/\partial x$ versus x and y at $t = 1155$ h ($t_r = 6.60$ h). The cross-shore MASS transect is indicated with a gray dashed line and $\bar{D} = 1$ ppb contour shown in black (*e.g.*, see Fig. 6). Location of moorings Tr (white, +) and W1 (yellow, o) and dye release (magenta dot) are also indicated.

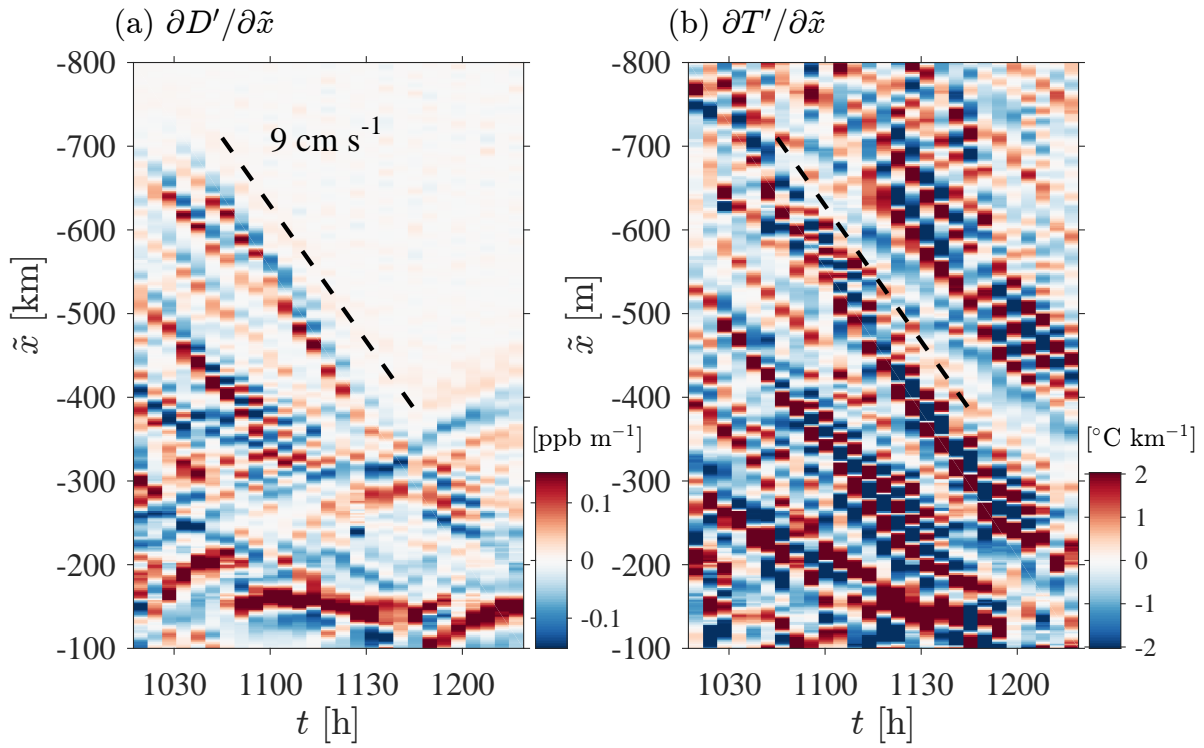


FIG. 14. Small-scale dye $\partial D'/\partial \tilde{x}$ (a) and temperature $\partial T'/\partial \tilde{x}$ (b) on cross-shore MASS transect (dashed line in Fig. 13) versus local, shoreline referenced cross-shore coordinate \tilde{x} and time t during deformation period. The dashed black line indicates an onshore progression of 9 cm s^{-1} .

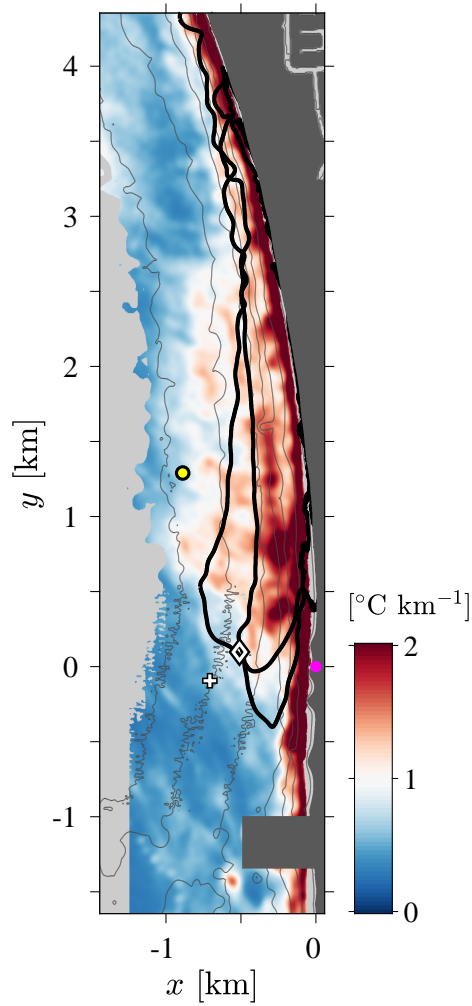


FIG. 15. Time root-mean-square of the cross-shore, small-scale temperature gradient $\text{rms}(\partial T'/\partial x)$ during the deformation period $1020 \leq t \leq 1217$ h. The rms estimate was derived from 27 MASS passes of surface $\partial T'/\partial x$, and regions with fewer than 25 samples were removed prior to applying the large-scale spatial filter described in Section 2d. Light gray are regions without data and the wake of the Imperial Beach pier at $y \approx -1$ km and land has been masked in dark gray.